Complex aneuploidy triggers autophagy and p53-mediated apoptosis and impairs the second lineage segregation in human preimplantation embryos

Marius Regin[1], Yingnan Lei[1], Edouard Couvreu De Deckersberg[1], Charlotte Janssens[1], Anfien Huyghebaert[1], Yves Guns[2], Pieter Verdyck[3], Greta Verheyen[2], Hilde Van de Velde[1,2], Karen Sermon[1,#], Claudia Spits[1,#,*]

[1]Research Group Genetics Reproduction and Development, Faculty of Medicine and Pharmacy, Vrije Universiteit Brussel, Laarbeeklaan 103, 1090 Jette, Brussels, Belgium

[2]Brussels IVF, Universitair Ziekenhuis Brussel, Laarbeeklaan 101, 1090 Jette, Brussels, Belgium

[3]Vrije Universiteit Brussel (VUB), Universitair Ziekenhuis Brussel (UZ Brussel), Clinical Sciences, Research Group Genetics Reproduction and Development, Centre for Medical Genetics, Brussels, Belgium

[#]These authors contributed equally to this work.

*Corresponding author: Claudia.Spits@vub.be

Abstract

About 70% of human cleavage stage embryos show chromosomal mosaicism, falling to 20% in blastocysts. Chromosomally mosaic human blastocysts can implant and lead to healthy new-borns with normal karyotypes. Studies in mouse embryos and human gastruloids have shown that aneuploid cells show proteotoxic stress, autophagy and p53 activation and that they are eliminated from the epiblast by apoptosis while being tolerated in the trophectoderm. These observations suggest a selective loss of aneuploid cells from human embryos, but the underlying mechanisms are not yet fully understood. In this study we investigated the cellular consequences of aneuploidy in a total of 125 human blastocysts. RNA-sequencing of trophectoderm cells showed transcriptional signatures of activated p53 pathway and apoptosis, which was proportionate to the level of chromosomal imbalance. Immunostaining corroborated that aneuploidy triggers proteotoxic stress, autophagy, p53-signalling, and apoptosis independent from DNA damage. Total cell numbers were lower in aneuploid embryos, due to a decline both in trophectoderm and in epiblast/primitive endoderm cell numbers. While lower cell numbers in trophectoderm may be attributed to apoptosis, it appeared that aneuploidy impaired the second lineage segregation, particularly primitive endoderm formation. This might be reinforced by retention of NANOG in aneuploid embryos. Our findings might explain why fully aneuploid embryos fail to further develop and we hypothesize that the same mechanisms lead to removal of aneuploid cells from mosaic embryos. This hypothesis needs further study as we did not analyze chromosomal mosaic embryos. Finally, we demonstrated a few differences with previous findings in the mouse, emphasizing the need for human embryo research to understand the consequences of aneuploidy.

Introduction

Aneuploidy is common in human preimplantation embryos from both natural (Munné et al., 2020a) and medically assisted reproduction cycles (Capalbo et al., 2021; Chavez et al., 2012; Chow et al., 2014; Fragouli et al., 2019; Johnson et al., 2010; Mertzanidou et al., 2013b, 2013a; Popovic et al., 2020; Starostik et al., 2020; Vanneste et al., 2009; Voullaire et al., 2000; Wells and Delhanty, 2000; Yang et al., 2021). Depending on the study, up to 80% of human cleavage stage embryos are found to be aneuploid, of which 70% show chromosomal mosaicism, i.e., the presence of at least two cell lineages with different genomic content (Regin et al., 2022). The reasons behind this high rate of chromosomal abnormalities of mitotic origin is still largely unknown (McCoy, 2017). One explanation is that cleavage-stage embryos have a weak spindle assembly checkpoint (SAC) that is uncoupled of apoptosis until the blastocyst stage (Jacobs et al., 2017; Vázquez-Diez et al., 2019), in combination with an abundancy of transcripts of anti-apoptotic genes (Yan et al., 2013). Only after embryonic genome activation, the rapidly increasing expression of pro-apoptotic genes along with the full functionality of the SAC establishes the control of mitotic errors. Additionally, aneuploidy in human embryos originates from an erroneous first mitotic division through a prolonged prometaphase (Currie et al., 2022).

It is by now well established that chromosomally mosaic embryos can result in healthy new-borns with normal karyotypes, implying a progressive and selective loss of aneuploid cells during development (Capalbo et al., 2021; Fragouli et al., 2019, 2017; Greco et al., 2015; Munné et al., 2020b, 2017; Viotti et al., 2021; Yang et al., 2021). In the preimplantation embryo, several studies have shown that the proportion of aneuploid cells within the embryo decreases as from three days post fertilization (3dpf) (Fragouli et al., 2019; van Echten-Arends et al., 2011; Yang et al., 2021) with no

apparent preferential allocation of aneuploid cells to either trophectoderm (TE) or inner cell mass (ICM) (Capalbo et al., 2013; Popovic et al., 2018; Ren et al., 2022; Starostik et al., 2020). Conversely, the TE of mouse embryos treated with the SAC inhibitor reversine show a similar but statistically significant 6% enrichment for aneuploid cells (Bolton et al., 2016). Similarly, other studies on human embryos found that the TE contained a slightly higher number of aneuploid cells than the ICM, but without reaching statistical significance (Griffin et al., 2022; Starostik et al., 2020). Lastly, aneuploid cells have also been found to be excluded as cell debris (Orvieto et al., 2020) or allocated to the blastocoel cavity and to peripheral cells that do not participate in the formation of the embryo (Griffin et al., 2022).

After implantation, aneuploid cells become progressively more frequent in the trophoblast lineage as compared to the epiblast (EPI) and primitive endoderm (PrE) (Starostik et al., 2020). This suggests that the trophoblast cells are more tolerant to aneuploidy, which is in line with the rate of 1-2% of confined placental mosaicism found in the general population (Kalousek and Vekemans, 1996). Large copy number variations appear to be mostly confined to placental lineages (Zamani Esteki et al., 2019) due to developmental bottlenecks occurring during the first lineage segregation which genetically isolate TE from ICM (Coorens et al., 2021). Taken together, there is ample evidence supporting the selective elimination of aneuploid cells from the embryonic lineage during pre- and post-implantation development, while the extraembryonic tissues appear to be more tolerant to genetic imbalances.

From a cellular point of view, aneuploidy has two types of consequences: a generic response and one that depends on the specific aneuploidy. The first type of response is highly conserved and has been found from yeast and plants to mouse and human cells (reviewed in: Santaguida and Amon, 2015; Zhu et al., 2018; Chunduri and

95 Storchová, 2019; Chunduri et al., 2022; Krivega et al., 2022). Aneuploidy results in
96 gene-dosage defects, leading to an unbalanced protein pool that induces the activation
97 of the mechanisms to restore protein homeostasis, such as the chaperone system, the
98 ubiquitin proteasome system and autophagy (Ariyoshi et al., 2016; Dürrbaum et al.,
99 2014; Santaguida et al., 2015; Stingele et al., 2012). If these systems are
100 overwhelmed, the accumulation of misfolded or aggregated proteins induces
101 proteotoxic stress which is detrimental to the cells (Donnelly et al., 2014; Huettel et al.,
102 2008; Ohashi et al., 2015; Oromendia et al., 2012; Stingele et al., 2012; Tang et al.,
103 2011; Torres et al., 2007; Williams et al., 2008). Further, aneuploidy can cause
104 replication stress, which in turn can lead to DNA-damage (Passerini et al., 2016;
105 Santaguida et al., 2017; Sheltzer et al., 2011), p53 activation (Li et al., 2010;
106 Santaguida et al., 2017; Thompson and Compton, 2010) and ultimately to cell cycle
107 arrest and apoptosis (reviewed in: Santaguida and Amon, 2015; Zhu et al., 2018; Regin
108 et al., 2022).

109 These mechanisms also appear to be active during early embryonic development and
110 to have a lineage specific effect. In mice, clearance of aneuploid cells by apoptosis
111 requires the activation of autophagy and p53 (Singla et al., 2020). Aneuploid cells are
112 only being eliminated by apoptosis in the ICM (Bolton et al., 2016) and at similar rates
113 in the EPI and the PrE (Singla et al., 2020). In a study using human 2D gastruloids with
114 reversine-induced aneuploidy, apoptosis was only induced in differentiating but not in
115 pluripotent cells, although aneuploidy did induce an increase in total nuclear p53 in
116 both cell types. Similarly, as in the mouse, the aneuploid cells were eliminated by
117 apoptosis from the embryonic germ layers but were tolerated in the TE-like cells (Yang
118 et al., 2021).

119 The type of aneuploidy and the percentage of aneuploid cells within a
120 euploid/aneuploid mosaic embryo determine its developmental capacity. The viability
121 of mouse embryos inversely correlates to the proportion of aneuploid cells, with 50%
122 of euploid cells being sufficient to sustain normal development (Bolton et al., 2016).
123 This same threshold appears to apply to human embryos, where embryos with less
124 than 50% of aneuploid cells have higher developmental potential than those containing
125 more than 50%, albeit both performing worse than fully euploid embryos (Viotti et al.,
126 2021, Capalbo et al., 2021).

127 Conversely, whole chromosome gains and losses that are present in every cell of the
128 human embryo are usually linked to lethality with the notable exception of trisomies 13
129 (Patau syndrome), 18 (Edwards syndrome) and 21 (Down syndrome), and sex
130 chromosome abnormalities. The effects of these imbalances can manifest already
131 during early embryo development (Fuchs Weizman et al., 2019; Licciardi et al., 2018;
132 Sanchez-Ribas et al., 2019; Shahbazi et al., 2020). Shahbazi *et al.* recently described
133 the consequences of carrying specific meiotic aneuploidies on human embryo
134 development using an in vitro implantation model (Shahbazi et al., 2020). They showed
135 that human embryos with trisomy 15, 16 and 21 and monosomy 21 readily all reached
136 the blastocyst stage, and that monosomy 21 embryos arrested after implantation while
137 trisomy 15 and 21 embryos developed further. Interestingly, trisomy 16 embryos
138 showed a hypoproliferative trophoblast due to excessive CDH1 expression, a gene
139 located on chromosome 16.

140 In this study, we investigated the cellular responses to complex aneuploidy during
141 human preimplantation development, with a focus on stress response and lineage
142 segregation events. We assessed previously unexplored general consequences of

143 naturally acquired aneuploidies in human embryos with focus on impaired lineage
144 segregation events.

145 **Methods**

146 **Ethical approval.** All experiments have been approved by the local Commission of
147 Medical Ethics of the UZ Brussel (B.U.N. 143201628722) and the Federal Committee
148 for Medical and Scientific Research on Human Embryos in vitro (AdV069 and AdV091).
149 Patients from Brussels IVF (UZ Brussel) donated their embryos for research after
150 written informed consent.

151 **Culture of human pre-implantation embryos.**

152 All human embryos, unless stated otherwise, were warmed using the Vitrification Thaw
153 Kit (Vit Kit-Thaw; Irvine Scientific, USA) and cultured in 25 µL droplets of Origio
154 Sequential Blast™ medium (Origio) at 37°C with 5% O_2, 6% CO_2 and 89% N_2. Embryos
155 were graded before vitrification by experienced clinical embryologists according to
156 Gardner and Schoolcraft criteria (Gardner and Schoolcraft, 1999).

157 **Experiment 1:** We warmed vitrified human blastocysts (5-6dpf) after PGT (28 euploid
158 and 22 aneuploid) or at 3dpf (n=11). Post PGT-embryos were left to recover for 2h in
159 culture medium, after which they underwent a second TE biopsy. For the reversine
160 experiment, we cultured the 3dpf embryos for 24h in culture medium supplemented
161 with 0.5 µM reversine (Stem Cell Technologies) and after wash-out we let them
162 develop until 5dpf and subsequently took a biopsy. The concentration of 0.5 µM
163 reversine was chosen based on previous experiments in mouse embryos (Bolton et
164 al., 2016; Singla et al., 2020).

165 **Experiment 2:** We warmed 12 vitrified and undiagnosed human blastocysts (5-6dpf)
166 of which 6 were cultured in culture medium for 16hrs. The other 6 embryos were
167 cultured in medium supplemented with 0.1mg/mL Bleomycin (Sigma-Aldrich) for 16hrs.

168 **Experiment 3:** We warmed vitrified human blastocysts (5-6dpf) after PGT (7 euploid
169 and 11 aneuploid) that were left to recover for 2hrs in culture medium.

170 **Experiment 4:** We warmed 5dpf-6dpf PGT embryos (10 euploid and 14 aneuploid)
171 and cultured them for 16h to ensure sufficient time to progress to the second lineage
172 differentiation. Prior to fixation we live-stained all the embryos with either Caspase-3/7
173 or Caspase-8 (Supplementary Table 9) for 30 min. Additionally, we warmed 5dpf-6dpf
174 PGT embryos (6 euploid and 4 aneuploid) and cultured them for 16h without live-
175 staining.

176 **Biopsy procedure.** The zona pellucida was opened (15-25μm) on 4dpf using a Saturn
177 Laser (Cooper Surgical). For PGT cycles, expanded good quality embryos were
178 biopsied on 5dpf; early blastocysts were evaluated again for expansion on 6dpf. Briefly,
179 embryos were transferred to HEPES buffered medium and biopsied on a Nikon
180 inversed microscope equipped with a Saturn Laser. The herniated TE cells were then
181 aspirated and cut using manual laser shoots. In case of sticking cells this was
182 supported by mechanical cutting. After successful tubing, the blastocysts were vitrified
183 using CBS-VIT High-Security straws (CryoBioSystem, L'Aigle, France) with
184 dimethylsulphoxide-ethylene glycol-sucrose as the cryoprotectants (Irvine Scientific
185 Freeze Kit, Newtownmountkennedy, County Wicklow, Ireland) (Van Landuyt et al.,
186 2011). The TE biopsy for RNA-sequencing (Experiment 1) was performed with the
187 same procedure, cells were biopsied from the same opening in the zona pellucida.

188 **PGT.** During PGT, our Center of Medical Genetics at the UZ Brussels analyzed a TE
189 sample with multiple cells for each embryo. Next Generation Sequencing: The
190 chromosomal analysis was performed by WGA (Sureplex, Illumina) followed by library
191 preparation (KAPA HyperPlus, Roche), sequencing on a NovaSeq (Illumina) and an
192 in-house developed interpretation pipeline. The analysis has an effective resolution of
193 5 Mb.

194 **SNP-array:** We relied on whole genome amplification (MDA, Repli-G) followed by
195 genome wide SNP array using Karyomapping (Vitrolife) with Bluefuse software
196 (Vitrolife). In addition, SNP array data were analyzed with an in-house developed
197 interpretation pipeline for aneuploidy detection.

198 **RNA-sequencing.** Multiple (5-10) TE cells were used as input to generate full length
199 cDNA with the SMART-SeqTM v4 UltraTM Low Input RNA Kit (Clontech Laboratories,
200 Inc.) according to the manufacturer's instructions. The quality of cDNA was checked
201 using the AATI Fragment Analyzer (Advances Analytical). Library preparation was
202 performed using the KAPA HyperPlus Library Preparation Kit (KAPA Biosystems)
203 according to the manufacturer's instructions. During cDNA synthesis and library
204 preparation we used 17 and 11 PCR cycles, respectively. Sequencing was performed
205 on a NovaSeq 6000 (Illumina) with 25 million reads per sample.

206 **Bioinformatics analysis.** Reads were trimmed using cutadapt version 1.11 to remove
207 the "QuantSEQ FWD" adaptor sequence. We checked the quality of the reads using
208 the FastQC algorithm (Love et al., 2014). Count tables were generated using STAR
209 (Dobin et al., 2013) (version 2.5.3) through mapping against the Genome Reference
210 Consortium Human Build 38 patch release 10 (GRCh38.p10) combined with a general
211 transfer format (GTF) file, both downloaded from the Ensembl database. The RNA-

212 sequencing by Expectation Maximization (RSEM) (Li and Dewey, 2011) software
213 (version 1.3.0) was used to produce the count tables.

214 Differential gene expression analysis was performed using R-studio (Version 1.1.456)
215 with the edgeR (Robinson et al., 2009) and limma (Ritchie et al., 2015) packages. We
216 included genes with a count per million greater than 1 in at least two samples. The
217 trimmed mean of M values (Robinson and Oshlack, 2010) algorithm was used for
218 normalization. The normalized counts were then transformed in a $\log_2$ fold-change
219 ($\log_2$FC) table with their associated statistics. In each comparison, genes with a |
220 $\log_2$FC | > 1 and an FDR < 0.05 were considered as significantly differentially
221 expressed.

222 Gene set enrichment analysis (GSEA) was performed using the GSEA software
223 (version 4.3.2) from the Molecular Signature Database (https://www.gsea-
224 msigdb.org/gsea/msigdb/index.jsp). We generated a ranked gene list based on the
225 normalized count matrix of the whole transcriptome that was detected after differential
226 gene expression. The ranked gene list was then subjected to the GSEA function, and
227 we searched the Hallmark and C2 library for significantly enriched pathways.
228 Significance was determined using a cut-off value of 25% FDR. This cut-off is proposed
229 in the user guide of the GSEA (https://www.gsea-
230 msigdb.org/gsea/doc/GSEAUserGuideTEXT.htm) especially for incoherent gene
231 expression datasets, as suggested by our PCAs, which allows for hypothesis driven
232 validation of the dataset.

233 The copy number variation (CNV) analysis was inferred from our RNA-sequencing
234 data set using inferCNV R package (version 1.7.1) (Inferring copy number alterations
235 from tumor single cell RNA-Seq data

236 (https://github.com/broadinstitute/inferCNV/wiki"). Our count table was used as input
237 and compared to the reference set which in our case was the expression data of the
238 euploid embryos. The analysis followed the standard workflow in inferCNV with the
239 following parameters: “denoise” mode, value of 1 was used for the “cutoff”, prediction
240 of CNV states using default Hidden Markov Models (HMM) method,
241 “cluster_by_groups” was set to TRUE, and other values were set by default.

242 **Gene dosage analysis.** We calculated the total number of loci with imbalanced gene
243 expression based on the genetic abnormalities identified during the PGT. For this, we
244 used the number of coding loci per chromosomal region as listed in the ENSMBL
245 database (ensemble.org) and included both gains and losses, either mosaic or
246 homogeneously present, and both full chromosomal aneuploidy as well as segmental
247 abnormalities. The embryos were ranked based on the total number of imbalanced loci
248 and separated into a low- and a high-imbalanced gene dosage group. The low-dosage
249 group contained the embryos with the lowest 50th percentile in number of unbalanced
250 loci, the high-dosage group the embryos with 50th percentile or higher.

251 **Immunocytochemistry.** Prior to fixation we removed the zona pellucida using pre-
252 warmed to 37°C Acidic Tyrode’s Solution (Sigma-Aldrich) for 30 sec – 2 min and
253 subsequently washed in PBS/2%BSA. Embryos were then fixed using 4%
254 paraformaldehyde (Sigma-Aldrich) for 10 min, washed three times in PBS/2%BSA for
255 5 min and then permeabilized using 0.1% Triton X-100 (Sigma-Aldrich) for 20 min
256 followed by another washing cycle. We used PBS/2% BSA supplemented with 10%
257 FBS for 1h to block non-specific protein binding. The embryos were then incubated
258 overnight with primary antibodies (Supplementary Table 9) diluted in blocking buffer at
259 4°C. The next day, they underwent another washing cycle using PBS/2%BSA and
260 were then incubated with secondary antibodies (1:200, Supplementary Table 9) for 1h

261 at room temperature. After washing, nuclei were stained using Hoechst 33342
262 (5µg/mL, Life Technologies) diluted in PBS/2%BSA for 15 min. For imaging we
263 mounted the embryos on poly-L-lysine coated glass slides (Sigma-Aldrich) in 3µL of
264 PBS. To avoid flattening of the embryos we used Secure-Seal^{TM} Spacers (9mm
265 diameter, 0.12mm deep, Thermofisher) before putting the coverslips in place. For the
266 experiments that required re-staining we imaged the embryos in 3µL PBS/2%BSA in
267 18 well µ-Slides (Ibidi) and subsequently recuperated them. After recuperation we
268 photobleached the embryos stained for CASP3/7 by using maximum laser power of
269 the 488 nm channel and maximum size of the pinhole for 10 min. The embryos were
270 then re-stained using rat anti-GATA4 primary antibody and the matching Alexa Fluor
271 488 secondary antibody (Supplementary Table 9) (to replace the CASP3/7 staining).

272 **Imaging and image analysis.** Confocal imaging was performed using the LSM800
273 (Zeiss). Z-stacks were taken with a LD C-Apochromat 40x/1.1 NA water immersion
274 objective in optical sections of 1µm. Nuclei were counted using the Blob finder function
275 of Arivis Vision 4D (3.4.0). All other measurements were performed using the Zen 2
276 (blue edition) or Image J software based on the optical sections and/or orthogonal
277 projections.

278 **Statistics.** The type of statistical test and p-values are mentioned in the figure legends.
279 For most comparisons we used one-way ANOVA or Student's t-test with or without
280 Welch's correction. For experiments that contained groups with small sample sizes we
281 used non-parametric tests (Mann-Whitney). Fisher-exact test was used to determine
282 the dependency of the ploidy status on the presence or absence of primitive endoderm.
283 We used GraphPad Prism 9.0.0 for statistical testing. The trend analysis regarding
284 gene dosage effects was performed with SPSS using the Jonckheere-Terpstra test.

285 **Results**

286 **Human embryos with complex aneuploidy show gene dosage defects and**
287 **transcriptomic signatures of p53 activation and apoptosis**

288 We first tested for the presence of a common transcriptomic response to different
289 complex aneuploidies. For this, we studied the transcriptome of a TE biopsy of fifty
290 human blastocysts (5 or 6dpf) previously diagnosed by Preimplantation Genetic
291 Testing (PGT) as either euploid or as containing an aneuploidy of at least two whole
292 chromosomes in all cases except for one embryo (further referred to as aneuploid,
293 detailed karyotypes can be found in the Supplementary Table 1). The aneuploidy was
294 presumed to have occurred during meiosis or during the first cleavage from zygote to
295 the 2-cell stage, resulting in all or most of the cells of the TE biopsy containing the
296 same genetic imbalances. We also included a TE sample of eleven human blastocysts
297 that were treated with 0.5 μM reversine from 3dpf to 4dpf, to induce complex mosaic
298 aneuploidy (referred to as reversine-treated embryos). Of these, 14 euploid, 20
299 aneuploid and 11 reversine-treated embryos yielded good quality RNA-sequencing
300 results.

301 Principal component analysis using all expressed genes revealed no clustering of the
302 euploid, aneuploid or reversine-treated embryos into distinct groups (Fig. 1a,
303 Supplementary Figure 1a). We used InferCNV
304 (https://github.com/broadinstitute/inferCNV/wiki) to bioinformatically infer the
305 chromosomal copy numbers based on the higher or lower expression of the genes
306 located on chromosomes with gains or losses (Fig. 1b, Supplementary Fig. 1b,c). We
307 compared the inferred karyotypes to those obtained during PGT and found a match for
308 45/48 of the full chromosome aneuploidies, while euploidy was correctly predicted in

309 all cases (Supplementary Fig. 1b). These results show that aneuploidy in human
310 blastocysts results in abnormal gene dosage effects. Of note, the karyotypes of the
311 reversine-treated embryos could not be determined since this drug induces different
312 aneuploidies in each cell, leading to mosaic TE biopsies. Also, the karyotypes of the
313 3dpf embryos were not determined by PGT before the reversine treatment. InferCNV
314 detected only a trisomy 12 in one of the reversine-treated embryos, likely of meiotic or
315 first-cleavage origin (Supplementary Figure 1c).

316 Despite the abnormal gene dosage, but in line with the lack of clear clustering in the
317 PCA, the differential gene expression analysis yielded 21 significantly upregulated and
318 2 downregulated genes (Fig. 1c, Supplementary Table 2). These findings are similar
319 to those of other studies on the transcriptome of aneuploid human embryonic cells,
320 which also found a few significantly deregulated genes (Fernandez Gallardo et al.,
321 2023; Groff et al., 2019; Martin et al., 2023; Maxwell et al., 2022). We next focused on
322 pathway analysis based on a ranked gene list of the whole transcriptome. We found
323 that cellular stress gene sets were positively enriched in the aneuploid samples,
324 including the p53-pathway and apoptosis (Fig. 1d-f). Gene sets related to metabolism,
325 translation, mitochondrial function and proliferation, such as translation and ribosome,
326 oxidative phosphorylation and MYC targets, were negatively enriched (Fig. 1d-f).

327 When comparing reversine-treated versus euploid embryos we found 34 significantly
328 upregulated and 22 significantly downregulated genes (Supplementary Fig 1d-f,
329 Supplementary Table 3). The expression profile differed from that identified in the
330 endogenously aneuploid embryos. Here, we found mitotic spindle, WNT-beta catenin
331 signalling, KRAS signalling and lysosome gene sets to be positively enriched while
332 oxidative phosphorylation, MYC targets, translation and ribosome were negatively
333 enriched. We found no evidence for p53 activation or apoptosis. This suggests that

334 naturally acquired aneuploidies of meiotic origin may elicit a different transcriptomic
335 response than reversine-induced mitotic aneuploidies, with a differential induction of
336 the p53 signalling pathway and apoptosis, and inhibition of proliferation.

337 **High gene-dosage imbalances result in high p53 activation and apoptosis while**
338 **low gene dosage imbalances induce pro-survival pathways**

339 To test whether there is a relationship between the type of cellular stress signatures
340 and the size of the chromosomal imbalances, as previously described in cancer cells
341 (Dürrbaum and Storchová, 2016), we categorized the aneuploid embryos into a low-
342 and a high- imbalanced gene dosage group. This separation was based on the total
343 number of coding loci that were affected by the aneuploidies (Supplementary Table 4).
344 The low-dosage group contained the embryos under the 50th percentile when ranking
345 the embryos from the lowest to the highest number of unbalanced loci. The high-
346 dosage group contained the embryos with 50th percentile or higher. Principal
347 component analysis showed that high-dosage embryos clustered separately from the
348 euploid embryos (Fig. 2a), with 65 significantly upregulated and 153 significantly
349 downregulated genes (Fig. 2b, Supplementary Table 5). High dosage embryos
350 showed a transcriptomic profile consistent with activation of the p53-pathway and
351 apoptosis, while the unfolded protein response, DNA-repair, MYC targets, oxidative
352 phosphorylation, translation and ribosome were inhibited (Fig. 2c-e).

353 In contrast, low-dosage embryos lacked separation from the euploid embryos in the
354 PCA (Fig. 2f) and only had one differentially expressed gene (Fig. 2g). While we still
355 found aneuploidy related stress responses such as p53-pathway and apoptosis to be
356 activated, we found also pro-survival gene sets such as MYC targets (Dang et al.,
357 2006; Wang et al., 2021), MTORC1 signalling (Hung et al., 2012), unfolded protein

358 response (Hetz et al., 2020; Zanetti et al., 2016) and hypoxia (Simões-Sousa et al.,
359 2018) to be enriched (Fig. 2h-j). Low-dosage embryos showed no profiles of ribosome
360 or translation impairment. Last, the plotting of the expression levels of genes in the p53
361 and apoptosis pathways show their progressive stronger induction or suppression from
362 euploid to low and high dosage embryos (Fig. 2k). This illustrates the association
363 between the severity of the protein pool imbalance and the induction of the cellular
364 stress response.

365 **Aneuploidy triggers proteotoxic stress, DNA-damage independent p53-**
366 **activation, autophagy and apoptosis**

367 To further investigate the cellular stress responses identified by the transcriptomic
368 analysis, we carried out immunostaining on the same embryos that underwent TE
369 biopsy for transcriptome analysis. The results show that aneuploid and reversine-
370 treated embryos have increased signal intensity of active CASP3/7 and CASP8 (Fig.
371 3a-d). Both aneuploid and reversine-treated embryos also have lower cell numbers
372 than euploid embryos, likely due to the apoptosis-mediated cell loss (Fig. 3e).

373 We next sought to corroborate the transcriptomic signatures of proteotoxic stress and
374 autophagy. The number of puncta per cell of LC3B, and p62, as well as the intensity
375 of HSP70 staining, as markers of autophagy and chronic protein misfolding, were
376 significantly increased in both aneuploid and reversine-treated embryos (Fig. 3f-j). We
377 also tested for the colocalization of CASP8 and HSP70 at the individual cell level. We
378 found that reversine-treated embryonic cells mainly co-express CASP8/HSP70, while
379 the minority is single positive for either CASP8 or HSP70 (Figure 3k,l). These results
380 show that although the transcriptomic profile of naturally occurring aneuploidies and

381 reversine-treated embryos is moderately different (Figure 1c-f, Supplementary Figure
382 1d-f), the downstream protein response is similar.

383 One of the key activated pathways identified during the transcriptome analysis was
384 p53-signalling. Thus, we sought to validate p53 activation by staining for the
385 phosphorylation of Serine-15 on p53, which is phosphorylated upon stimuli such as
386 DNA-damage and metabolic stress (Loughery et al., 2014). We found that indeed
387 aneuploid embryos showed a higher percentage of cells with activated p53 (Fig. 3m,n).
388 These differences did not reach significance when considering the ICM/EPI-OCT4-
389 positive cells or TE OCT4-negative cells separately (Supplementary Fig. 2a-c)
390 probably due to insufficient statistical power.

391 We then stained an additional batch of embryos (Supplementary Table 6) for the
392 double-strand break marker gH2AX, with the aim of determining if the p53 activation
393 was DNA-damage mediated. As a control, we treated human embryos with the DNA-
394 damage inducer Bleomycin and compared them to untreated embryos. All cells of
395 Bleomycin treated embryos showed a pan-nuclear gH2AX pattern, while untreated
396 embryos rarely showed cells containing foci (Fig. 3o). Euploid and aneuploid embryos
397 showed similar fractions of cells with gH2AX foci or pan-nuclear staining (Fig. 3p,q),
398 which did not change when dividing the aneuploid embryos into high and low dosage
399 groups, (Fig. 3r).

400 Lastly, the transcriptome analysis showed significant upregulation in aneuploid and
401 high-dosage aneuploid embryos of the gene *DRAM1* (DNA Damage Regulated
402 Autophagy Modulator-1, Figure 2b). DRAM1 is in the lysosomal membrane, and it
403 increases autophagic flux and apoptosis after stress-induced p53 activation in cancer
404 cells (Crighton et al., 2006; Guan et al., 2015). We stained euploid and aneuploid

405 embryos (Supplementary Table 6) for DRAM1 and NANOG and found that the
406 expression of DRAM1 is increased specifically in the cytoplasm of aneuploid TE cells
407 but not in the ICM (NANOG-positive cells, Figure 3s,t).

408 **Aneuploidy increases apoptosis in the trophectoderm and impairs lineage**
409 **segregation events**

410 We next investigated whether the stress responses to aneuploidy are cell-type specific,
411 as shown in the mouse (Bolton et al., 2016; Singla et al., 2020) and human 2D
412 gastruloids (Yang et al., 2021). Concretely, we aimed to study the consequences of
413 aneuploidy during the first lineage segregation event to TE and ICM, and the second
414 lineage segregation event to EPI and PrE.

415 We first immunostained euploid and aneuploid 5-6dpf human embryos for the
416 pluripotency marker NANOG (Supplementary Table 6). NANOG protein was enriched
417 in the nuclei of aneuploid TE and ICM cells (Fig. 4a,b), which could suggest a delay in
418 the exit from pluripotency in both lineages. We then co-stained 6-7dpf euploid and
419 aneuploid blastocysts for OCT4, CASP3/7 and LC3B (Supplementary Table 7).
420 Overall, we found lower cell counts in both the TE (OCT-negative cells) and in the
421 OCT4-positive cells (ICM/EPI cells), Fig. 4c-e) of aneuploid embryos. This resulted in
422 lower total cell numbers in aneuploid embryos (Fig. 4f), in line with our previous
423 observation (Fig. 3e). We found a higher percentage of nuclear CASP3/7 positive cells
424 (Fig. 4g,h) as well as a higher CASP3/7 mean intensity per cell (Fig. 4g,i) specifically
425 in the TE of aneuploid embryos. In contrast, not a single OCT4-positive cell of either
426 the euploid or aneuploid embryos showed nuclear CASP3/7 signal (Fig. 4g). Aneuploid
427 embryos also showed a higher number of CASP3/7-positive micronuclei in the cells
428 (Fig. 4j,k). The lineage-specific response to aneuploidy also extended to presence of

429 autophagy. The staining for LC3B showed that aneuploid embryos displayed overall
430 increased levels of autophagy which was mainly taking place in the TE and not the
431 ICM (Fig. 4l-o).

432 Finally, we observed that the counts of OCT4-positive cells in the aneuploid embryos
433 distributed in two groups: one with very low counts and one with counts in the range of
434 that of euploid embryos (Fig. 4e). This led us to hypothesize that some of the aneuploid
435 embryos had a delayed ICM development, with impairment of the second lineage
436 segregation event. All blastocysts analyzed above were re-stained for GATA4 (PrE
437 marker) and imaged together with OCT4 (ICM/EPI marker). We found that while all
438 euploid embryos contained GATA4-positive cells, 39% of aneuploid embryos had no
439 GATA4-positive cells (Fig. 4p,q). Furthermore, in those aneuploid embryos that
440 contained GATA4-positive PrE cells, there was a significantly lower ratio of GATA4-
441 positive to OCT4-positive/GATA4-negative cells (Fig. 4r). Categorization of the
442 aneuploid embryos into a low- and a high-dosage group (Supplementary Table 8)
443 showed that the higher the number of imbalanced loci, the lower the cell numbers in
444 the TE and PrE but not in the EPI (Fig. 4s).

445 Taken together, these results suggest that there are important differences in how the
446 embryonic lineages respond to aneuploidy. While the TE is activating autophagy and
447 apoptosis, this is not the case for the ICM/EPI. In turn, while in both lineages,
448 aneuploidy appears to promote a delay in the downregulation of NANOG during
449 differentiation, the ICM of high-dosage aneuploid embryos frequently has poor or no
450 differentiation to PrE.

451 **Discussion**

452 In this work, we studied the consequences of uniform complex aneuploidy in human
453 preimplantation embryos. In our study we find that, while aneuploid embryos had lower
454 cell numbers in both TE and ICM/EPI, the effect of aneuploidy was cell-type
455 dependent. Aneuploid TE presented transcriptomic signatures of p53 signalling and
456 apoptosis, and immunostaining of whole embryos showed that aneuploidy results in
457 increased proteotoxic stress, autophagy, activated p53 independent from DNA-
458 damage and subsequent apoptosis. In contrast, in the ICM, aneuploidy affects PrE
459 formation.

460 Overall, our gene-expression results are in line with previously published RNA-
461 sequencing studies on aneuploid human embryonic cells that identified transcriptional
462 signatures consistent with an alteration of cell proliferation (Martin et al., 2023; Maxwell
463 et al., 2022; Starostik et al., 2020), the cell cycle (Fuchs Weizman et al., 2019; Licciardi
464 et al., 2018; Martin et al., 2023; Starostik et al., 2020; Vera-Rodriguez et al., 2015),
465 deregulation of autophagy (Licciardi et al., 2018; Sanchez-Ribas et al., 2019), p53
466 signalling (Licciardi et al., 2018) and apoptosis (Groff et al., 2019; Licciardi et al., 2018;
467 Martin et al., 2023; Maxwell et al., 2022; Sanchez-Ribas et al., 2019).

468 We found that strength of these transcriptomic alterations is dependent of the number
469 of imbalanced genes. These gene-dosage dependent effects of aneuploidy are akin to
470 those extensively reported in human and mouse aneuploid cancer cell lines (Dürrbaum
471 and Storchová, 2016). We found that higher numbers of aneuploid loci led to stronger
472 induction of p53 target genes and apoptosis responses in the TE cells. Interestingly,
473 high-dosage aneuploid embryos displayed an inhibited unfolded protein response, as
474 also seen in aneuploid embryonic cells by another study (Fernandez Gallardo et al.,

475 2023), while this pathway was activated in low dosage aneuploid embryos. These
476 results suggest that while low-dosage aneuploid cells are trying to restore homeostasis
477 by the unfolded protein response (Hetz et al., 2020; Jäger et al., 2012; Li and Zhu,
478 2022), high-dosage aneuploid cells are past this point and undergo apoptosis by p53
479 activation.

480 In the subsequent experiments, we found that aneuploid embryos showed increased
481 signal of early (CASP8) and late (CASP3/7) caspases, indicating activation of the
482 extrinsic apoptotic pathway (McIlwain et al., 2013). The higher levels of p62 and LC3B
483 we found in these embryos suggests that this activation of apoptosis results at least in
484 part from a sustained interaction between p62, LC3B and CASP8 (Pan et al., 2011).
485 In parallel, aneuploid embryos showed evidence of an activated p53 pathway, not only
486 on a transcriptomic level, but also by presenting elevated levels of Serine 15
487 phosphorylated p53 (Loughery et al., 2014). This p53 activation has been previously
488 observed on a transcriptomic level in another study on human embryos (Licciardi et
489 al., 2018) and was identified as a key mediator of aneuploidy-dependent apoptosis in
490 the mouse (Singla et al., 2020). While ATM-mediated phosphorylation of p53 on S15
491 has been reported in cancer cell lines as a consequence of DNA damage during
492 chromosome mis-segregation (Janssen et al., 2011), we found no evidence of
493 increased levels of DNA-damage in our cohort of embryos. It is worth noting that
494 studies on constitutionally aneuploid cell lines have shown contradicting results, with
495 some studies finding p53 activation (Li et al., 2010; Thompson and Compton, 2010)
496 and others not (Tang et al., 2011). An alternative route for p53 activation is through
497 p38, a sensor for cellular stress such as endoplasmic reticulum stress (Mishra and
498 Karande, 2014; Thompson and Compton, 2010). Metabolic alterations might also
499 promote ATM mediated activation of p53 (Li et al., 2010) or phosphorylation on Serine

500 15 (Jones et al., 2005). Our study also identified *DRAM1* as a significantly upregulated
501 gene in aneuploid embryos. *DRAM1* is directly regulated by p53 and is not only able
502 to regulate autophagic flux but it also regulates apoptosis, making it likely an important
503 downstream effector of the p53-mediated effects of aneuploidy in human embryos
504 (Crighton et al., 2006; Guan et al., 2015). Lastly, it is worth considering that the
505 complex abnormal human embryonic cells present in our sample might have been
506 subjected to mitotic stress, as suggested by the enrichment of mitotic spindle pathway
507 genes observed in the RNA-seq dataset. Mitotic stress might be induced by sustained
508 proteotoxic stress (Zhu et al., 2018) and can further have contributed to p53 activation.
509 Based on this evidence, we propose that the p53 activation we observed in the
510 embryos with presumed meiotic aneuploidy is akin to that of constitutionally aneuploid
511 cells, and not due to DNA-damage but to cellular stress caused by proteotoxic stress.
512 Taken together, the increased levels of apoptosis we find in aneuploid embryos appear
513 to be mediated at least by two pathways: the sustained p62/LC3B mediated response
514 to unfolded proteins and by p53 activation as a response to cellular stress. An
515 interesting observation from the apoptosis stainings is that aneuploid embryos
516 contained increased numbers of CASP3/7 positive micronuclei. This is similar to
517 findings in a non-human primate model showing that abnormal chromosomes can be
518 encapsulated in micronuclei, which can subsequently be selectively eliminated from
519 the embryo (Daughtry et al., 2019). The presence of DNA in the cytoplasm has also
520 recently been observed during live-imaging of human embryos, which occurs during
521 blastocyst expansion due to nuclear DNA shedding (Domingo-Muelas *et al.*, 2023). In
522 human cleavage stage embryos these micronuclei have been shown to contain genetic
523 material that originates from chromosome breakages due to replication fork stalling
524 and DNA-damage (Palmerola et al., 2022).

525 In the second part of our work, we focused on studying the lineage-specific response
526 to complex aneuploidy, as the studies on reversine-treated mouse embryos (Bolton et
527 al., 2016; Singla et al., 2020) and human 2D gastruloids (Yang et al., 2021) also
528 identified a cell-type specific effect of aneuploidy. In the mouse, aneuploid cells are
529 eliminated by apoptosis in the EPI, while tolerated in the TE, and in human 2D
530 gastruloids, aneuploid cells are eliminated in the post-gastrulation embryonic germ
531 layers but tolerated in the TE. In the human embryo, the first lineage segregation is
532 established at 5dpf, and the ICM and TE are marked by the differential expression of
533 NANOG and GATA3 (Gerri et al., 2020; Meistermann et al., 2021; Allègre et al., 2022;
534 Regin et al., 2023). We found that both aneuploid ICM and TE cells showed nuclear
535 enrichment of NANOG, which can be suggestive of a delay or impairment of the first
536 lineage segregation event, possibly due to failure or delay in the exit from pluripotency
537 (Zhang et al., 2016).
538 While we found increased apoptosis in the aneuploid TE, we found that the ICM/EPI
539 had no CASP3/7 positive cells, despite showing lower cell numbers than the euploid
540 ICM/EPI. These results are in line with the findings of Martin and colleagues, where
541 the RNA-sequencing of TE and ICM samples showed disrupted regulation of apoptosis
542 in mosaic aneuploid TE cells while the ICM showed primarily deregulated
543 mitochondrial function (Martin et al., 2023). In contrast, while the study of Victor et al
544 also finds increased apoptosis in the aneuploid TE, some of their embryos did present
545 CASP3/7 positive signals in the ICM. Further research will be needed to understand if
546 the differences with our findings and those of Martin et al are related to technical or to
547 biological factors. A potential explanation for the lack of apoptosis in the human
548 ICM/EPI could be due to an uncoupling between aneuploidy-induced stress signals
549 and apoptosis, as observed in human embryonic stem cells (Mantel et al., 2007). In
550 this context, the lower cell numbers in the aneuploid ICM/EPI could be explained by

551 other known effects of *p53* activation next to induction of apoptosis. First, *p53*
552 activation can decrease cell proliferation, leading to lower cell numbers. Secondly, *p53*
553 activation can downregulate *NANOG* expression (Abdelalim and Tooyama, 2014; Lin
554 et al., 2005), potentially leading to loss of pluripotency and driving the cells to
555 differentiation and out of the ICM/EPI.

556 Another observation was that while the aneuploid TE had increased levels of
557 autophagy markers and DRAM1 expression, this did not reach statistical significance
558 in the ICM/EPI. This aligns with work on human embryos showing absence of
559 activation of p53-signalling and autophagy in the transcriptome of the ICM of mosaic
560 human embryos (Martin et al., 2023) , but is in contrast with the reversine-treated
561 mouse embryos and human gastruloids, showing increased autophagy and p53
562 signalling in the ICM lineages (Singla et al., 2020; Yang et al., 2021). Next to a species-
563 specific effect, it is possible that the difference between the mouse, human gastruloid
564 and human studies are because the reversine treatment used had direct effects on
565 p53 (D'Alise et al., 2008; S Santaguida, 2010), leading to the activation of autophagy
566 across the entire cells.

567 Finally, we found that in those embryos that had already undergone the second lineage
568 segregation event, the aneuploid embryos had a significantly lower ratio of PrE
569 (GATA4-positive) to EPI (OCT4-positive/GATA4-negative) cells than euploid embryos,
570 suggesting that aneuploidy has a negative effect on PrE formation. Interestingly, recent
571 work comparing the gene-expression of euploid and mosaic aneuploid embryos has
572 also found that euploid embryos have a higher expression of the PrE marker *SOX17,*
573 (Martin et al., 2023).

574 While in mice, apoptosis is common during PrE formation to eliminate misallocated
575 cells through cell competition (Hashimoto and Sasaki, 2019; Plusa et al., 2008), our
576 data and that of others suggest that the human ICM rarely undergoes apoptosis, even
577 in karyotypically aberrant cells (Martin et al., 2023; Victor et al., 2019; Yang et al.,
578 2021). While a possible explanation suggested by our NANOG stainings is that in
579 aneuploid human embryos the PrE forms later due to retention of NANOG in the ICM
580 and TE, the mechanisms behind this second lineage differentiation defect remain to
581 be elucidated.

582 When interpreting the results of this study, it is important to bear in mind that we
583 identified the ICM/EPI as staining positive for OCT4 and the PrE as positive for GATA4.
584 We confirmed that the embryos analysed were expanded blastocysts which had
585 undergone the first lineage segregations, as OCT4 was restricted to the inner cells and
586 absent in TE cells (Niakan and Eggan, 2013). The identity of human ICM and EPI cells
587 is currently under vigorous debate (Meistermann et al., 2021; Radley et al., 2022) and
588 exclusive markers of either cell type are untested. Therefore, we cannot assign ICM or
589 EPI identity to OCT4-positive cells with certainty. However, in blastocysts with GATA4-
590 positive cells the second lineage segregation had occurred and PrE was established,
591 and consequently we confidently assigned the EPI identity to OCT4-positive cells in
592 these blastocysts. In GATA4-negative embryos OCT4-positive cells could be either
593 ICM or EPI cells. Interestingly, we only found a single GATA4-positive cell lacking
594 OCT4, supporting the hypothesis that PrE cells differentiate from EPI cells
595 (Meistermann et al., 2021).

596 Our study has several limitations and there are some considerations to bear in mind.
597 In this work, we did not analyse the transcriptome of the ICM, because the remaining
598 embryos were used for immunostaining after TE biopsy, and we can therefore not draw

599 any conclusions on the ICM transcriptome. We did not study embryos with the same
600 type of aneuploidy and can thus not provide insight on chromosome-specific effects.
601 Although some of our embryos carried genetic abnormalities in mosaic form as part of
602 their complex karyotype (aneuploid/aneuploid mosaics), we did not study
603 diploid/aneuploid mosaic embryos and can therefore not assert that these also activate
604 the same cellular stress pathways in their aneuploid cells. Since these pathways are
605 common to most cell types, our prediction would however be that they are activated in
606 mosaic embryos too. The possibilities for functional studies and lineage tracing
607 experiments in human embryos are very limited, which is why we can only present an
608 observational study. Alternatively, in silico modelling data could be leveraged to
609 address the roles of aneuploidy in blastocyst formation and development (Nissen et
610 al., 2017). The gene-expression analysis revealed that embryos with naturally acquired
611 and induced aneuploidies had few deregulated pathways in common, with mainly the
612 mitotic spindle genes being differentially expressed in both. Conversely, we used
613 reversine to induce aneuploidy in the immunostaining experiments to increase the
614 sample size, and the results showed that the reversine-induced aneuploidies elicited
615 the same stress responses as aneuploidy. This suggests that while reversine-based
616 models are very close, they may not fully mimic endogenous aneuploidy. An alternative
617 is to use the SAC-inhibitor A3146, recently proposed by the Zernicka-Goetz group to
618 induce low-degree aneuploidy in mouse embryos (Sanchez-Vasquez et al., 2023).
619 Finally, our results on the activation of autophagy and proteotoxic stress are also
620 limited by experimental constraints. We cannot rule out indirect activation of apoptosis
621 mediated by autophagy due to the degradation of cell organelles (Gump and Thorburn,
622 2011). Also, other upstream regulators of autophagy could be involved, such as the
623 cGAS-STING pathway (Krivega et al., 2021). While we and others (Singla et al., 2020)
624 used HSP70 as a marker for chronic protein misfolding, we cannot preclude that is

625 also acts as a (temporary) suppressor of the extrinsic apoptosis pathway in aneuploid
626 cells (Gabai et al., 2002; Lanneau et al., 2008).

627 Taken together, our results show that while the same pathways appear to be activated
628 in human and mouse embryos with complex aneuploidy, human embryos have a
629 dosage-dependent and differential response when it comes to the downstream effect
630 of these pathways in the different cell lineages. While the mouse readily depletes
631 aneuploid cells by apoptosis specifically from the embryonic lineage before
632 implantation (Bolton et al., 2016; Singla et al., 2020), in the human embryo, apoptosis
633 appears to be more active in the TE and aneuploidy negatively affects PrE formation
634 in the ICM. Our results provide insight into the mechanisms by which human embryos
635 respond to gene-dosage imbalances and may contribute to understanding how
636 aneuploid cells are selectively eliminated in mosaic preimplantation embryos. Further
637 research, especially by using human embryos with endogenous chromosomal
638 mosaicism, will be needed to shed light on the interactions between proteotoxic stress,
639 the p53 pathway and differentiation during early development, for which the most novel
640 models of human embryo implantation (Deglincerti et al., 2016; Kagawa et al., 2021;
641 Shahbazi et al., 2020, 2016) will prove to be of incalculable value.

642

643

644

645

646 **References**

647 Abdelalim EM, Tooyama I. 2014. Knockdown of p53 suppresses Nanog expression in
648 embryonic stem cells. *Biochem Biophys Res Commun* **443**:652–657.
649 doi:10.1016/J.BBRC.2013.12.030
650 Allègre N, Chauveau S, Dennis C, Renaud Y, Meistermann D, Estrella LV, Pouchin P,
651 Cohen-Tannoudji M, David L, Chazaud C. 2022. NANOG initiates epiblast fate
652 through the coordination of pluripotency genes expression. *Nature*
653 *Communications 2022 13:1* **13**:1–13. doi:10.1038/s41467-022-30858-8
654 Ariyoshi K, Miura T, Kasai K, Fujishima Y, Oshimura M, Yoshida MA. 2016. Induction
655 of genomic instability and activation of autophagy in artificial human aneuploid
656 cells. *Mutat Res* **790**:19–30. doi:10.1016/J.MRFMMM.2016.06.001
657 Bolton H, Graham SJL, Van Der Aa N, Kumar P, Theunis K, Fernandez Gallardo E,
658 Voet T, Zernicka-Goetz M. 2016. Mouse model of chromosome mosaicism reveals
659 lineage-specific depletion of aneuploid cells and normal developmental potential.
660 *Nat Commun* **7**:1–12. doi:10.1038/ncomms11165
661 Capalbo A, Poli M, Rienzi L, Girardi L, Patassini C, Fabiani M, Cimadomo D, Benini F,
662 Farcomeni A, Cuzzi J, Rubio C, Albani E, Sacchi L, Vaiarelli A, Figliuzzi M, Findikli
663 N, Coban O, Boynukalin FK, Vogel I, Hoffmann E, Livi C, Levi-setti PE, Ubaldi FM,
664 Simo C. 2021. Mosaic human preimplantation embryos and their developmental
665 potential in a prospective , non-selection clinical trial 1–10.
666 doi:10.1016/j.ajhg.2021.11.002
667 Capalbo A, Wright G, Elliott T, Ubaldi FM, Rienzi L, Nagy ZP. 2013. FISH reanalysis
668 of inner cell mass and trophectoderm samples of previously array-CGH screened
669 blastocysts shows high accuracy of diagnosis and no major diagnostic impact of
670 mosaicism at the blastocyst stage. *Human Reproduction* **28**:2298–2307.
671 doi:10.1093/humrep/det245
672 Chavez SL, Loewke KE, Han J, Moussavi F, Colls P, Munne S, Behr B, Reijo Pera RA.
673 2012. Dynamic blastomere behaviour reflects human embryo ploidy by the four-
674 cell stage. *Nat Commun* **3**. doi:10.1038/NCOMMS2249
675 Chow JFC, Yeung WSB, Lau EYL, Lee VCY, Ng EHY, Ho PC. 2014. Array
676 comparative genomic hybridization analyses of all blastomeres of a cohort of
677 embryos from young IVF patients revealed significant contribution of mitotic errors
678 to embryo mosaicism at the cleavage stage. *Reprod Biol Endocrinol* **12**.
679 doi:10.1186/1477-7827-12-105
680 Chunduri NK, Barthel K, Storchova Z. 2022. Consequences of Chromosome Loss:
681 Why Do Cells Need Each Chromosome Twice? *Cells 2022, Vol 11, Page 1530*
682 **11**:1530. doi:10.3390/CELLS11091530
683 Chunduri NK, Storchová Z. 2019. The diverse consequences of aneuploidy. *Nat Cell*
684 *Biol*. doi:10.1038/s41556-018-0243-8
685 Coorens THH, Oliver TRW, Sanghvi R, Sovio U, Cook E, Vento-Tormo R, Haniffa M,
686 Young MD, Rahbari R, Sebire N, Campbell PJ, Charnock-Jones DS, Smith GCS,
687 Behjati S. 2021. Inherent mosaicism and extensive mutation of human placentas.
688 *Nature* **592**:80–85. doi:10.1038/s41586-021-03345-1
689 Crighton D, Wilkinson S, O'Prey J, Syed N, Smith P, Harrison PR, Gasco M, Garrone
690 O, Crook T, Ryan KM. 2006. DRAM, a p53-Induced Modulator of Autophagy, Is
691 Critical for Apoptosis. *Cell* **126**:121–134. doi:10.1016/j.cell.2006.05.034
692 Currie CE, Ford E, Benham Whyte L, Taylor DM, Mihalas BP, Erent M, Marston AL,
693 Hartshorne GM, McAinsh AD. 2022. The first mitotic division of human embryos
694 is highly error prone. *Nat Commun* **13**. doi:10.1038/S41467-022-34294-6

D'Alise AM, Amabile G, Iovino M, Di Giorgio FP, Bartiromo M, Sessa F, Villa F, Musacchio A, Cortese R. 2008. Reversine, a novel Aurora kinases inhibitor, inhibits colony formation of human acute myeloid leukemia cells. *Mol Cancer Ther* **7**:1140–1149. doi:10.1158/1535-7163.MCT-07-2051

Dang C V., O'Donnell KA, Zeller KI, Nguyen T, Osthus RC, Li F. 2006. The c-Myc target gene network. *Semin Cancer Biol* **16**:253–264. doi:10.1016/J.SEMCANCER.2006.07.014

Daughtry BL, Rosenkrantz JL, Lazar NH, Fei SS, Redmayne N, Torkenczy KA, Adey A, Yan M, Gao L, Park B, Nevonen KA, Carbone L, Chavez SL. 2019. Single-cell sequencing of primate preimplantation embryos reveals chromosome elimination via cellular fragmentation and blastomere exclusion. *Genome Res* **29**:367–382. doi:10.1101/gr.239830.118

David K Gardner, William B Schoolcraft. 1999. Culture and transfer of human blastocysts. *Curr Opin Obstet Gynecol* **11**:307–311.

Deglincerti A, Croft GF, Pietila LN, Zernicka-Goetz M, Siggia ED, Brivanlou AH. 2016. Self-organization of the in vitro attached human embryo. *Nature* **533**:251–254. doi:10.1038/nature17948

Dobin A, Davis CA, Schlesinger F, Drenkow J, Zaleski C, Jha S, Batut P, Chaisson M, Gingeras TR. 2013. STAR: ultrafast universal RNA-seq aligner. *Bioinformatics* **29**:15–21. doi:10.1093/bioinformatics/bts635

Donnelly N, Passerini V, Dürrbaum M, Stingele S, Storchová Z. 2014. HSF1 deficiency and impaired HSP90-dependent protein folding are hallmarks of aneuploid human cells. *EMBO J* **33**:2374. doi:10.15252/EMBJ.201488648

Dürrbaum M, Kuznetsova A, Passerini V, Stingele S, Stoehr G, Storchová Z. 2014. Unique features of the transcriptional response to model aneuploidy in human cells. *BMC Genomics* **15**:139. doi:10.1186/1471-2164-15-139

Dürrbaum M, Storchová Z. 2016. Effects of aneuploidy on gene expression: implications for cancer. *FEBS J* **283**:791–802. doi:10.1111/FEBS.13591

Fernandez Gallardo E, Sifrim A, Chappell J, Demeulemeester J, Herrmann JC, Vermotte R, Kerremans A, Van Der Haegen M, Herck J Van, Vanuytven S, Vandereyken K, Macaulay IC, Vermeesch JR, Peeraer K, Debrock S, Pasque V, Voet T, Affiliations #. 2023. A multi-omics genome-and-transcriptome single-cell atlas of human preimplantation embryogenesis reveals the cellular and molecular impact of chromosome instability. *bioRxiv* 2023.03.08.530586. doi:10.1101/2023.03.08.530586

Fragouli E, Alfarawati S, Spath K, Babariya D, Tarozzi N, Borini A, Wells D. 2017. Analysis of implantation and ongoing pregnancy rates following the transfer of mosaic diploid–aneuploid blastocysts. *Hum Genet* **136**:805–819. doi:10.1007/s00439-017-1797-4

Fragouli E, Munne S, Wells D. 2019. The cytogenetic constitution of human blastocysts: insights from comprehensive chromosome screening strategies. *Hum Reprod Update* **25**:15–33. doi:10.1093/humupd/dmy036

Fuchs Weizman N, Wyse BA, Antes R, Ibarrientos Z, Sangaralingam M, Motamedi G, Kuznyetsov V, Madjunkova S, Librach CL. 2019. Towards Improving Embryo Prioritization: Parallel Next Generation Sequencing of DNA and RNA from a Single Trophectoderm Biopsy. *Sci Rep* **9**:1–11. doi:10.1038/s41598-019-39111-7

Gabai VL, Mabuchi K, Mosser DD, Sherman MY. 2002. Hsp72 and Stress Kinase c-jun N-Terminal Kinase Regulate the Bid-Dependent Pathway in Tumor Necrosis Factor-Induced Apoptosis. *Mol Cell Biol* **22**:3415. doi:10.1128/MCB.22.10.3415-3424.2002

745 Gerri C, McCarthy A, Alanis-Lobato G, Demtschenko A, Bruneau A, Loubersac S,
746 Fogarty NME, Hampshire D, Elder K, Snell P, Christie L, David L, Van de Velde
747 H, Fouladi-Nashta AA, Niakan KK. 2020. Initiation of a conserved trophectoderm
748 program in human, cow and mouse embryos. *Nature* **587**:443–447.
749 doi:10.1038/S41586-020-2759-X
750 Greco E, Minasi MG, Fiorentino F. 2015. Healthy Babies after Intrauterine Transfer of
751 Mosaic Aneuploid Blastocysts. *New England Journal of Medicine* **373**:2089–2090.
752 doi:10.1056/NEJMc1500421
753 Griffin DK, Brezina PR, Tobler K, Zhao Y, Silvestri G, Mccoy RC, Anchan R, Benner
754 A, Cutting GR, Kearns WG. 2022. The human embryonic genome is karyotypically
755 complex, with chromosomally abnormal cells preferentially located away from the
756 developing fetus. *Human Reproduction*. doi:10.1093/HUMREP/DEAC238
757 Groff AF, Resetkova N, DiDomenico F, Sakkas D, Penzias A, Rinn JL, Eggan K. 2019.
758 RNA-seq as a tool for evaluating human embryo competence. *Genome Res*
759 **29**:1705–1718. doi:10.1101/gr.252981.119
760 Guan JJ, Zhang XD, Sun W, Qi L, Wu JC, Qin ZH. 2015. DRAM1 regulates apoptosis
761 through increasing protein levels and lysosomal localization of BAX. *Cell Death*
762 *Dis* **6**:e1624–e1624. doi:10.1038/cddis.2014.546
763 Gump JM, Thorburn A. 2011. Autophagy and apoptosis: what is the connection?
764 *Trends Cell Biol* **21**:387–392. doi:10.1016/J.TCB.2011.03.007
765 Hashimoto M, Sasaki H. 2019. Epiblast Formation by TEAD-YAP-Dependent
766 Expression of Pluripotency Factors and Competitive Elimination of Unspecified
767 Cells. *Dev Cell* **50**:139-154.e5. doi:10.1016/J.DEVCEL.2019.05.024
768 Hetz C, Zhang K, Kaufman RJ. 2020. Mechanisms, regulation and functions of the
769 unfolded protein response. *Nature Reviews Molecular Cell Biology 2020 21:8*
770 **21**:421–438. doi:10.1038/s41580-020-0250-z
771 Huettel B, Kreil DP, Matzke M, Matzke AJM. 2008. Effects of aneuploidy on genome
772 structure, expression, and interphase organization in Arabidopsis thaliana. *PLoS*
773 *Genet* **4**. doi:10.1371/JOURNAL.PGEN.1000226
774 Hung CM, Garcia-Haro L, Sparks CA, Guertin DA. 2012. mTOR-Dependent Cell
775 Survival Mechanisms. *Cold Spring Harb Perspect Biol* **4**.
776 doi:10.1101/CSHPERSPECT.A008771
777 Jacobs K, Van de Velde H, De Paepe C, Sermon K, Spits C. 2017. Mitotic spindle
778 disruption in human preimplantation embryos activates the spindle assembly
779 checkpoint but not apoptosis until Day 5 of development. *MHR: Basic science of*
780 *reproductive medicine* **23**:321–329. doi:10.1093/molehr/gax007
781 Jäger R, Bertrand MJM, Gorman AM, Vandenabeele P, Samali A. 2012. The unfolded
782 protein response at the crossroads of cellular life and death during endoplasmic
783 reticulum stress. *Biol Cell* **104**:259–270. doi:10.1111/BOC.201100055
784 Janssen A, Van Der Burg M, Szuhai K, Kops GJPL, Medema RH. 2011. Chromosome
785 segregation errors as a cause of DNA damage and structural chromosome
786 aberrations. *Science* **333**:1895–1898. doi:10.1126/SCIENCE.1210214
787 Johnson DS, Cinnioglu C, Ross R, Filby A, Gemelos G, Hill M, Ryan A, Smotrich D,
788 Rabinowitz M, Murray MJ. 2010. Comprehensive analysis of karyotypic
789 mosaicism between trophectoderm and inner cell mass. *MHR: Basic science of*
790 *reproductive medicine* **16**:944–949. doi:10.1093/molehr/gaq062
791 Jones RG, Plas DR, Kubek S, Buzzai M, Mu J, Xu Y, Birnbaum MJ, Thompson CB.
792 2005. AMP-activated protein kinase induces a p53-dependent metabolic
793 checkpoint. *Mol Cell* **18**:283–293. doi:10.1016/J.MOLCEL.2005.03.027
794 Kagawa H, Javali A, Khoei HH, Sommer TM, Sestini G, Novatchkova M, Scholte op
795 Reimer Y, Castel G, Bruneau A, Maenhoudt N, Lammers J, Loubersac S, Freour

796 T, Vankelecom H, David L, Rivron N. 2021. Human blastoids model blastocyst
797 development and implantation. *Nature* 1–9. doi:10.1038/s41586-021-04267-8
798 Kalousek DK, Vekemans M. 1996. Confined placental mosaicism. *J Med Genet*.
799 doi:10.1136/jmg.33.7.529
800 Krivega M, Stiefel CM, Karbassi S, Andersen LL, Chunduri NK, Donnelly N, Pichlmair
801 A, Storchová Z. 2021. Genotoxic stress in constitutive trisomies induces
802 autophagy and the innate immune response via the cGAS-STING pathway.
803 *Communications Biology 2021 4:1* **4**:1–16. doi:10.1038/s42003-021-02278-9
804 Krivega M, Stiefel CM, Storchova Z. 2022. Consequences of chromosome gain: A new
805 view on trisomy syndromes. *Am J Hum Genet*. doi:10.1016/j.ajhg.2022.10.014
806 Lanneau D, Brunet M, Frisan E, Solary E, Fontenay M, Garrido C. 2008. Heat shock
807 proteins: essential proteins for apoptosis regulation. *J Cell Mol Med* **12**:743.
808 doi:10.1111/J.1582-4934.2008.00273.X
809 Li B, Dewey CN. 2011. RSEM: accurate transcript quantification from RNA-Seq data
810 with or without a reference genome. *BMC Bioinformatics* **12**:323.
811 Li M, Fang X, Baker DJ, Guo L, Gao X, Wei Z, Han S, Van Deursen JM, Zhang P.
812 2010. The ATM-p53 pathway suppresses aneuploidy-induced tumorigenesis.
813 *Proc Natl Acad Sci U S A* **107**:14188–14193.
814 doi:10.1073/PNAS.1005960107/SUPPL_FILE/PNAS.201005960SI.PDF
815 Li R, Zhu J. 2022. Effects of aneuploidy on cell behaviour and function. *Nature Reviews*
816 *Molecular Cell Biology 2022 23:4* **23**:250–265. doi:10.1038/s41580-021-00436-9
817 Licciardi F, Lhakhang T, Kramer YG, Zhang Y, Heguy A, Tsirigos A. 2018. Human
818 blastocysts of normal and abnormal karyotypes display distinct transcriptome
819 profiles. *Sci Rep* **8**:1–9. doi:10.1038/s41598-018-33279-0
820 Lin T, Chao C, Saito S, Mazur SJ, Murphy ME, Appella E, Xu Y. 2005. p53 induces
821 differentiation of mouse embryonic stem cells by suppressing Nanog expression.
822 *Nat Cell Biol* **7**:165–171. doi:10.1038/NCB1211
823 Loughery J, Cox M, Smith LM, Meek DW. 2014. Critical role for p53-serine 15
824 phosphorylation in stimulating transactivation at p53-responsive promoters.
825 *Nucleic Acids Res* **42**:7666–7680. doi:10.1093/nar/gku501
826 Love MI, Huber W, Anders S. 2014. Moderated estimation of fold change and
827 dispersion for RNA-seq data with DESeq2. *Genome Biol* **15**. doi:10.1186/s13059-
828 014-0550-8
829 Mantel C, Guo Y, Lee MR, Kim M-K, Han M-K, Shibayama H, Fukuda S, Yoder MC,
830 Pelus LM, Kim K-S, Broxmeyer HE. 2007. Checkpoint-apoptosis uncoupling in
831 human and mouse embryonic stem cells: a source of karyotpic instability. *Blood*
832 **109**:4518–4527. doi:10.1182/blood-2006-10
833 Martin A, Mercader A, Dominguez F, Quiñonero A, Perez M, Gonzalez-Martin R,
834 Delgado A, Mifsud A, Pellicer A, De Los Santos MJ. 2023. Mosaic results after
835 preimplantation genetic testing for aneuploidy may be accompanied by changes
836 in global gene expression. *Front Mol Biosci* **10**:264.
837 doi:10.3389/FMOLB.2023.1180689
838 Maxwell SM, Lhakhang TC, Lin Z, Kramer YG, Zhang Y, Wang F, Heguy A, Tsirigos
839 A, Grifo JA, Licciardi F. 2022. Investigation of Global Gene Expression of Human
840 Blastocysts Diagnosed as Mosaic using Next-generation Sequencing.
841 *Reproductive Sciences* 1–11. doi:10.1007/s43032-022-00899-x
842 McCoy RC. 2017. Mosaicism in Preimplantation Human Embryos: When
843 Chromosomal Abnormalities Are the Norm. *Trends in Genetics* **33**:448–463.
844 doi:10.1016/J.TIG.2017.04.001
845 McIlwain DR, Berger T, Mak TW. 2013. Caspase Functions in Cell Death and Disease.
846 *Cold Spring Harb Perspect Biol* **5**:1–28. doi:10.1101/CSHPERSPECT.A008656

847 Meistermann D, Bruneau A, Loubersac S, Reignier A, Firmin J, François-Campion V,
848 Kilens S, Lelièvre Y, Lammers J, Feyeux M, Hulin P, Nedellec S, Bretin B, Castel
849 G, Allègre N, Covin S, Bihouée A, Soumillon M, Mikkelsen T, Barrière P, Chazaud
850 C, Chappell J, Pasque V, Bourdon J, Fréour T, David L. 2021. Integrated
851 pseudotime analysis of human pre-implantation embryo single-cell transcriptomes
852 reveals the dynamics of lineage specification. *Cell Stem Cell* **28**:1625-1640.e6.
853 doi:10.1016/j.stem.2021.04.027
854 Mertzanidou A, Spits C, Nguyen HT, Van de Velde H, Sermon K. 2013a. Evolution of
855 aneuploidy up to Day 4 of human preimplantation development. *Human*
856 *Reproduction* **28**:1716–1724. doi:10.1093/humrep/det079
857 Mertzanidou A, Wilton L, Cheng J, Spits C, Vanneste E, Moreau Y, Vermeesch JR,
858 Sermon K. 2013b. Microarray analysis reveals abnormal chromosomal
859 complements in over 70% of 14 normally developing human embryos. *Human*
860 *Reproduction* **28**:256–264. doi:10.1093/humrep/des362
861 Mishra R, Karande AA. 2014. Endoplasmic Reticulum Stress-Mediated Activation of
862 p38 MAPK, Caspase-2 and Caspase-8 Leads to Abrin-Induced Apoptosis. *PLoS*
863 *One* **9**:e92586. doi:10.1371/JOURNAL.PONE.0092586
864 Munné S, Blazek J, Large M, Martinez-Ortiz PA, Nisson H, Liu E, Tarozzi N, Borini A,
865 Becker A, Zhang J, Maxwell S, Grifo J, Babariya D, Wells D, Fragouli E. 2017.
866 Detailed investigation into the cytogenetic constitution and pregnancy outcome of
867 replacing mosaic blastocysts detected with the use of high-resolution next-
868 generation sequencing. *Fertil Steril* **108**:62-71.e8.
869 doi:10.1016/j.fertnstert.2017.05.002
870 Munné S, Nakajima ST, Najmabadi S, Sauer M V., Angle MJ, Rivas JL, Mendieta L V.,
871 MacAso TM, Sawarkar S, Nadal A, Choudhary K, Nezhat C, Carson SA, Buster
872 JE. 2020a. First PGT-A using human in vivo blastocysts recovered by uterine
873 lavage: Comparison with matched IVF embryo controls. *Human Reproduction*
874 **35**:70–80. doi:10.1093/humrep/dez242
875 Munné S, Spinella F, Grifo J, Zhang J, Beltran MP, Fragouli E, Fiorentino F. 2020b.
876 Clinical outcomes after the transfer of blastocysts characterized as mosaic by high
877 resolution Next Generation Sequencing- further insights. *Eur J Med Genet*
878 **63**:103741. doi:10.1016/j.ejmg.2019.103741
879 Niakan KK, Eggan K. 2013. Analysis of human embryos from zygote to blastocyst
880 reveals distinct gene expression patterns relative to the mouse. *Dev Biol* **375**:54–
881 64. doi:10.1016/J.YDBIO.2012.12.008
882 Nissen SB, Perera M, Gonzalez JM, Morgani SM, Jensen MH, Sneppen K, Brickman
883 JM, Trusina A. 2017. Four simple rules that are sufficient to generate the
884 mammalian blastocyst. *PLoS Biol* **15**:e2000737.
885 doi:10.1371/JOURNAL.PBIO.2000737
886 Ohashi A, Ohori M, Iwai K, Nakayama Y, Nambu T, Morishita D, Kawamoto T,
887 Miyamoto M, Hirayama T, Okaniwa M, Banno H, Ishikawa T, Kandori H, Iwata K.
888 2015. Aneuploidy generates proteotoxic stress and DNA damage concurrently
889 with p53-mediated post-mitotic apoptosis in SAC-impaired cells. *Nat Commun*
890 **6**:1–16. doi:10.1038/ncomms8668
891 Oromendia AB, Dodgson SE, Amon A. 2012. Aneuploidy causes proteotoxic stress in
892 yeast. *Genes Dev* **26**:2696–2708. doi:10.1101/gad.207407.112
893 Orvieto R, Shimon C, Rienstein S, Jonish-Grossman A, Shani H, Aizer A. 2020. Do
894 human embryos have the ability of self-correction? *Reprod Biol Endocrinol* **18**.
895 doi:10.1186/S12958-020-00650-8
896 Palmerola KL, Amrane S, De Los Angeles A, Xu S, Wang N, de Pinho J, Zuccaro M
897 V, Taglialatela A, Massey DJ, Turocy J, Robles A, Subbiah A, Prosser B, Lobo R,

898 Ciccia A, Koren A, Baslan T, Egli D. 2022. Replication stress impairs chromosome
899 segregation and preimplantation development in human embryos. *Cell*.
900 doi:10.1016/j.cell.2022.06.028
901 Pan J-A, Ullman E, Dou Z, Zong W-X. 2011. Inhibition of protein degradation induces
902 apoptosis through a microtubule-associated protein 1 light chain 3-mediated
903 activation of caspase-8 at intracellular membranes. *Mol Cell Biol* **31**:3158–70.
904 doi:10.1128/MCB.05460-11
905 Passerini V, Ozeri-Galai E, De Pagter MS, Donnelly N, Schmalbrock S, Kloosterman
906 WP, Kerem B, Storchová Z. 2016. The presence of extra chromosomes leads to
907 genomic instability. *Nat Commun* **7**. doi:10.1038/NCOMMS10754
908 Plusa B, Piliszek A, Frankenberg S, Artus J, Hadjantonakis AK. 2008. Distinct
909 sequential cell behaviours direct primitive endoderm formation in the mouse
910 blastocyst. *Development* **135**:3081–3091. doi:10.1242/DEV.021519
911 Popovic M, Dhaenens L, Boel A, Menten B, Heindryckx B. 2020. Chromosomal
912 mosaicism in human blastocysts: The ultimate diagnostic dilemma. *Hum Reprod*
913 *Update* **26**:313–334. doi:10.1093/humupd/dmz050
914 Popovic M, Dheedene A, Christodoulou C, Taelman J, Dhaenens L, Van Nieuwerburgh
915 F, Deforce D, Van Den Abbeel E, De Sutter P, Menten B, Heindryckx B. 2018.
916 Chromosomal mosaicism in human blastocysts: The ultimate challenge of
917 preimplantation genetic testing? *Human Reproduction* **33**:1342–1354.
918 doi:10.1093/humrep/dey106
919 Radley A, Corujo-Simon E, Nichols J, Smith A, Dunn SJ. 2022. Entropy sorting of
920 single-cell RNA sequencing data reveals the inner cell mass in the human pre-
921 implantation embryo. *Stem Cell Reports* **0**. doi:10.1016/j.stemcr.2022.09.007
922 Regin M, Essahib W, Demtschenko A, Dewandre D, David L, Gerri C, Niakan KK,
923 Verheyen G, Tournaye H, Sterckx J, Sermon K, Van De Velde H. 2023. Lineage
924 segregation in human pre-implantation embryos is specified by YAP1 and TEAD1.
925 *Human Reproduction* **38**:1484–1498. doi:10.1093/HUMREP/DEAD107
926 Regin M, Spits C, Sermon K. 2022. On the origins and fate of chromosomal
927 abnormalities in human preimplantation embryos: an unsolved riddle. *Mol Hum*
928 *Reprod*. doi:10.1093/molehr/gaac011
929 Ren Y, Yan Z, Yang M, Keller L, Zhu X, Lian Y, Liu Q, Li R, Zhai F, Nie Y, Yan L, Smith
930 GD, Qiao J. 2022. Regional and developmental characteristics of human embryo
931 mosaicism revealed by single cell sequencing. *PLoS Genet* **18**.
932 doi:10.1371/journal.pgen.1010310
933 Ritchie ME, Phipson B, Wu D, Hu Y, Law CW, Shi W, Smyth GK. 2015. Limma powers
934 differential expression analyses for RNA-sequencing and microarray studies.
935 *Nucleic Acids Res* **43**:e47. doi:10.1093/nar/gkv007
936 Robinson MD, McCarthy DJ, Smyth GK. 2009. edgeR: A Bioconductor package for
937 differential expression analysis of digital gene expression data. *Bioinformatics*
938 **26**:139–140. doi:10.1093/BIOINFORMATICS/BTP616
939 Robinson MD, Oshlack A. 2010. A scaling normalization method for differential
940 expression analysis of RNA-seq data. doi:10.1186/gb-2010-11-3-r25
941 S Santaguida ATADSTAM. 2010. Dissecting the role of MPS1 in chromosome
942 biorientation and the spindle checkpoint through the small molecule inhibitor
943 reversine. *J Cell Biol* **190**:73–87.
944 Sanchez-Ribas I, Diaz-Gimeno P, Sebastián-León P, Mercader A, Quiñonero A,
945 Ballesteros A, Pellicer A, Domínguez F. 2019. Transcriptomic behavior of genes
946 associated with chromosome 21 aneuploidies in early embryo development. *Fertil*
947 *Steril* **111**:991-1001.e2. doi:10.1016/j.fertnstert.2019.01.023

Sanchez-Vasquez E, Bronner ME, Zernicka-Goetz M. 2023. HIF1A contributes to the survival of aneuploid and mosaic pre-implantation embryos. *bioRxiv* 2023.09.04.556218. doi:10.1101/2023.09.04.556218

Santaguida S, Amon A. 2015. Short- and long-term effects of chromosome mis-segregation and aneuploidy. *Nat Rev Mol Cell Biol*. doi:10.1038/nrm4025

Santaguida S, Richardson A, Iyer DR, M'Saad O, Zasadil L, Knouse KA, Wong YL, Rhind N, Desai A, Amon A. 2017. Chromosome Mis-segregation Generates Cell-Cycle-Arrested Cells with Complex Karyotypes that Are Eliminated by the Immune System. *Dev Cell* **41**:638-651.e5. doi:10.1016/J.DEVCEL.2017.05.022

Santaguida S, Vasile E, White E, Amon A. 2015. Aneuploidy-induced cellular stresses limit autophagic degradation. *Genes Dev* **29**:2010–2021. doi:10.1101/gad.269118.115

Shahbazi MN, Jedrusik A, Vuoristo S, Recher G, Hupalowska A, Bolton V, Fogarty NME, Campbell A, Devito LG, Ilic D, Khalaf Y, Niakan KK, Fishel S, Zernicka-Goetz M. 2016. Self-organization of the human embryo in the absence of maternal tissues. *Nat Cell Biol* **18**:700–708. doi:10.1038/ncb3347

Shahbazi MN, Wang T, Tao X, Weatherbee BAT, Sun L, Zhan Y, Keller L, Smith GD, Pellicer A, Scott RT, Seli E, Zernicka-Goetz M. 2020. Developmental potential of aneuploid human embryos cultured beyond implantation. *Nat Commun* **11**:1–15. doi:10.1038/s41467-020-17764-7

Sheltzer JM, Blank HM, Pfau SJ, Tange Y, George BM, Humpton TJ, Brito IL, Hiraoka Y, Niwa O, Amon A. 2011. Aneuploidy drives genomic instability in yeast. *Science (1979)* **333**:1026–1030. doi:10.1126/SCIENCE.1206412/SUPPL_FILE/1206412-SHELTZER.SOM.PDF

Simões-Sousa S, Littler S, Thompson SL, Minshall P, Whalley H, Bakker B, Belkot K, Moralli D, Bronder D, Tighe A, Spierings DCJ, Bah N, Graham J, Nelson L, Green CM, Foijer F, Townsend PA, Taylor SS. 2018. The p38α Stress Kinase Suppresses Aneuploidy Tolerance by Inhibiting Hif-1α. *Cell Rep* **25**:749-760.e6. doi:10.1016/J.CELREP.2018.09.060

Singla S, Iwamoto-Stohl LK, Zhu M, Zernicka-Goetz M. 2020. Autophagy-mediated apoptosis eliminates aneuploid cells in a mouse model of chromosome mosaicism. *Nat Commun* **11**:1–15. doi:10.1038/s41467-020-16796-3

Starostik MR, Sosin OA, McCoy RC. 2020. Single-cell analysis of human embryos reveals diverse patterns of aneuploidy and mosaicism. *Genome Res* **30**:814–826. doi:10.1101/gr.262774.120

Stingele S, Stoehr G, Peplowska K, Cox J, Mann M, Storchova Z. 2012. Global analysis of genome, transcriptome and proteome reveals the response to aneuploidy in human cells. *Mol Syst Biol* **8**:608. doi:10.1038/msb.2012.40

Tang YC, Williams BR, Siegel JJ, Amon A. 2011. Identification of Aneuploidy-Selective Antiproliferation Compounds. *Cell* **144**:499–512. doi:10.1016/J.CELL.2011.01.017

Thompson SL, Compton DA. 2010. Proliferation of aneuploid human cells is limited by a p53-dependent mechanism. *J Cell Biol* **188**:369–381. doi:10.1083/JCB.200905057

Torres EM, Sokolsky T, Tucker CM, Chan LY, Boselli M, Dunham MJ, Amon A. 2007. Effects of aneuploidy on cellular physiology and cell division in haploid yeast. *Science (1979)* **317**:916–924. doi:10.1126/SCIENCE.1142210/SUPPL_FILE/TORRES.SOM.PDF

van Echten-Arends J, Mastenbroek S, Sikkema-Raddatz B, Korevaar JC, Heineman MJ, van der Veen F, Repping S. 2011. Chromosomal mosaicism in human

998 preimplantation embryos: a systematic review. *Hum Reprod Update* **17**:620–627.
999 doi:10.1093/humupd/dmr014
1000 Van Landuyt L, Stoop D, Verheyen G, Verpoest W, Camus M, Van De Velde H,
1001 Devroey P, Van Den Abbeel E. 2011. Outcome of closed blastocyst vitrification in
1002 relation to blastocyst quality: Evaluation of 759 warming cycles in a single-embryo
1003 transfer policy. *Human Reproduction* **26**:527–534. doi:10.1093/humrep/deq374
1004 Vanneste E, Voet T, Le Caignec C, Ampe M, Konings P, Melotte C, Debrock S, Amyere
1005 M, Vikkula M, Schuit F, Fryns J-P, Verbeke G, D'Hooghe T, Moreau Y, Vermeesch
1006 JR. 2009. Chromosome instability is common in human cleavage-stage embryos.
1007 *Nat Med* **15**:577–583. doi:10.1038/nm.1924
1008 Vázquez-Diez C, Paim LMG, FitzHarris G. 2019. Cell-Size-Independent Spindle
1009 Checkpoint Failure Underlies Chromosome Segregation Error in Mouse Embryos.
1010 *Current Biology* **29**:865-873.e3. doi:10.1016/j.cub.2018.12.042
1011 Vera-Rodriguez M, Chavez SL, Rubio C, Pera RAR, Simon C. 2015. Prediction model
1012 for aneuploidy in early human embryo development revealed by single-cell
1013 analysis. *Nat Commun* **6**:7601. doi:10.1038/ncomms8601
1014 Victor AR, Tyndall JC, Brake AJ, Lepkowsky LT, Murphy AE, Griffin DK, McCoy RC,
1015 Barnes FL, Zouves CG, Viotti M. 2019. One hundred mosaic embryos transferred
1016 prospectively in a single clinic: exploring when and why they result in healthy
1017 pregnancies. *Fertil Steril* **111**:280–293. doi:10.1016/j.fertnstert.2018.10.019
1018 Viotti M, Victor AR, Barnes FL, Zouves CG, Besser AG, Grifo JA, Cheng EH, Lee MS,
1019 Horcajadas JA, Corti L, Fiorentino F, Spinella F, Minasi MG, Greco E, Munné S.
1020 2021. Using outcome data from one thousand mosaic embryo transfers to
1021 formulate an embryo ranking system for clinical use. *Fertil Steril* **115**:1212–1224.
1022 doi:10.1016/j.fertnstert.2020.11.041
1023 Voullaire L, Slater H, Williamson R, Wilton L. 2000. Chromosome analysis of
1024 blastomeres from human embryos by using comparative genomic hybridization.
1025 *Hum Genet* **106**:210–7.
1026 Wang C, Zhang J, Yin J, Gan Y, Xu S, Gu Y, Huang W. 2021. Alternative approaches
1027 to target Myc for cancer treatment. *Signal Transduction and Targeted Therapy*
1028 *2021 6:1* **6**:1–14. doi:10.1038/s41392-021-00500-y
1029 Wells D, Delhanty JD. 2000. Comprehensive chromosomal analysis of human
1030 preimplantation embryos using whole genome amplification and single cell
1031 comparative genomic hybridization. *Mol Hum Reprod* **6**:1055–62.
1032 Williams BR, Prabhu VR, Hunter KE, Glazier CM, Whittaker CA, Housman DE, Amon
1033 A. 2008. Aneuploidy affects proliferation and spontaneous immortalization in
1034 mammalian cells. *Science* **322**:703–709. doi:10.1126/SCIENCE.1160058
1035 Yan L, Yang M, Guo H, Yang L, Wu J, Li Rong, Liu P, Lian Y, Zheng X, Yan J, Huang
1036 J, Li M, Wu X, Wen L, Lao K, Li Ruiqiang, Qiao J, Tang F. 2013. Single-cell RNA-
1037 Seq profiling of human preimplantation embryos and embryonic stem cells. *Nat*
1038 *Struct Mol Biol* **20**:1131–1139. doi:10.1038/nsmb.2660
1039 Yang M, Rito T, Metzger J, Naftaly J, Soman R, Hu J, Albertini DF, Barad DH, Brivanlou
1040 AH, Gleicher N. 2021. Depletion of aneuploid cells in human embryos and
1041 gastruloids. *Nat Cell Biol* **23**:314–321. doi:10.1038/s41556-021-00660-7
1042 Zamani Esteki M, Viltrop T, Tšuiko O, Tiirats A, Koel M, Nõukas M, Žilina O, Teearu K,
1043 Marjonen H, Kahila H, Meekels J, Söderström-Anttila V, Suikkari AM, Tiitinen A,
1044 Mägi R, Kõks S, Kaminen-Ahola N, Kurg A, Voet T, Vermeesch JR, Salumets A.
1045 2019. In vitro fertilization does not increase the incidence of de novo copy number
1046 alterations in fetal and placental lineages. *Nat Med*. doi:10.1038/s41591-019-
1047 0620-2

1048 Zanetti M, Rodvold JJ, Mahadevan NR. 2016. The evolving paradigm of cell-
1049 nonautonomous UPR-based regulation of immunity by cancer cells. *Oncogene*
1050 **35**:269–278. doi:10.1038/ONC.2015.108
1051 Zhang M, Cheng L, Jia Y, Liu G, Li C, Song S, Bradley A, Huang Y. 2016. Aneuploid
1052 embryonic stem cells exhibit impaired differentiation and increased neoplastic
1053 potential. *EMBO J* **35**:2285–2300. doi:10.15252/EMBJ.201593103
1054 Zhu J, Tsai HJ, Gordon MR, Li R. 2018. Cellular Stress Associated with Aneuploidy.
1055 *Dev Cell*. doi:10.1016/j.devcel.2018.02.002
1056
1057

1058 **Data availability**

1059 Data are available from the corresponding author upon reasonable request. Files are
1060 stored at the Open Science Framework (OSF) and can be accessed through the
1061 identifier: osf.io/tc248. At OSF we provided for Figure 1, 2 and Supplementary Figure
1062 1 the input and output of the GSEA for each comparison. Also, source data files are
1063 provided for figures 3 and 4 and Supplementary Figure 2. We also provide the Prism
1064 file for all comparisons in which significancy was tested. Raw RNA-sequencing files
1065 are not provided due to GDPR guidelines concerning human embryo research.
1066 However, count tables generated from the raw data files are included in the source
1067 data files.

1068 **Acknowledgements**

1069 The authors would like to thank Marleen Carlé from the Center for Medical Genetics
1070 (UZ Brussel) for assisting during the tubing of trophectoderm samples, Hanne Vlieghe
1071 (UCLouvain, Brussels) for the validation of antibodies and the reversine reagent,
1072 Wilfried Cools from the Biostatistics and Medical Informatics Group (VUB) for the
1073 statistical advice and the members of the BRIGHTcore facility (UZ Brussel) for
1074 performing the RNA sequencing. We thank Prof. Rajiv McCoy for the scientific input
1075 and data exchange. This study was funded by the Fonds for Scientific Research in
1076 Flanders -G017218N- (Fonds Wetenschappelijk Onderzoek – Vlaanderen [FWO]).
1077 M.R., E.C.D.D. and C.J. are doctoral fellows at the FWO with grant numbers
1078 (1133622N, 1S73521N and 11H9823N, respectively). Y.L. is a predoctoral fellow
1079 supported by the China Scholarship Council (CSC)

1080

Author contributions

M.R. carried out all the experiments unless stated otherwise, interpreted, and analyzed the results, revised, and co-wrote the manuscript. Y.L. and E.C.D.D. performed bioinformatics analyses. C.J. contributed to immunostaining experiments during the revision. A.H. contributed to quantifications during the revision. Y.G. performed the trophectoderm biopsies. P.V. provided and supervised the diagnoses of the PGT embryos. G.V. and H.V.D.V. provided the embryos for this study. K.S. interpreted and supervised the experimental work and co-wrote the manuscript. C.S. designed, interpreted and supervised the experimental work and co-wrote the manuscript. All co-authors proofread the manuscript.

Competing interests

The authors declare no competing interests.

Fig. 1: RNA-sequencing of trophectoderm cells reveals gene dosage defects and transcriptomic signatures of p53 activation and apoptosis

a. Principal component analysis after transcriptome analysis of aneuploid versus euploid embryos. T= Trisomy, M=Monosomy. **b**. Comparison between the diagnosis of aneuploid embryos obtained after PGT (list on the left) and the results obtained after using InferCNV after RNA-sequencing (plot on the right). Red and blue indicate gain or loss of the chromosome, respectively. **c**. Volcano plot after differential gene expression analysis with a cutoff value of $|\log_2 \text{fold change}| > 1$ and $-\log_{10}(\text{FDR}) < 0.05$ for aneuploid versus euploid embryos showing 21 upregulated and 2 downregulated genes. **d.** Barplot of enriched Hallmark pathways after gene set enrichment analysis of aneuploid versus euploid embryos using a cut-off value of 25% FDR. **e.** Barplot of TOP20 enriched C2 library pathways after gene set enrichment analysis of aneuploid versus euploid embryos using a cut-off value of 25% FDR. **f.** Enrichment plots of p53-pathway, mitotic spindle, oxidative phosphorylation, MYC targets V1 and ribosome, showing up- or downregulation of genes that are part of the corresponding pathway. Source of all embryos: Experiment 1.

Fig. 2: Human embryos with the highest number of genes with abnormal copy number show stronger p53 pathway and apoptosis response.

a. Principal component analysis after transcriptome analysis of high-dosage aneuploid versus euploid embryos. T= Trisomy, M=Monosomy. **b**. Volcano plot after differential gene expression analysis with a cutoff value of $|\log_2 \text{fold change}| > 1$ and $-\log_{10}(\text{FDR}) < 0.05$ for high-dosage aneuploid versus euploid embryos showing 65 upregulated and 153 downregulated genes. **c.** Barplot of enriched Hallmark pathways after gene set enrichment analysis of high-dosage aneuploid versus euploid embryos using a cut-off value of 25% FDR. **d.** Barplot of TOP20 enriched C2 library pathways after gene set enrichment analysis of high-dosage aneuploid versus euploid embryos using a cut-off value of 25% FDR. **e.** Enrichment plots of p53-pathway, mitotic spindle, unfolded protein response, MYC targets V1 and oxidative phosphorlation, showing up- or downregulation of genes that are part of the corresponding pathway. **f**. Principal component analysis after transcriptome analysis of low-dosage aneuploid versus euploid embryos. T= Trisomy, M=Monosomy. **g**. Volcano plot after differential gene expression analysis with a cutoff value of $|\log_2 \text{fold change}| > 1$ and $-\log_{10}(\text{FDR}) < 0.05$ for low-dosage aneuploid versus euploid embryos showing 1 upregulated and 0 downregulated genes. **h.** Barplot of enriched Hallmark pathways after gene set enrichment analysis of low-dosage aneuploid versus euploid embryos using a cut-off value of 25% FDR. **i.** Barplot of enriched C2 library pathways after gene set enrichment analysis of low-dosage aneuploid versus euploid embryos using a cut-off value of 25% FDR. **j.** Enrichment plots of p53-pathway, mitotic spindle, MYC targets V1, unfolded protein response and hypoxia showing upregulation of genes that are part of the corresponding pathway. **k.** Violin plots with box and whisker plots of the counts per million mapped reads of a supervised set of 10 that are part of apoptosis (*BAD,*

BCL2L1, TNFRSF10B), p53 pathway (*DRAM1, MDM2, CDKN1A*), and DNA-damage (*DDB2*). *p = 0.027, **p = 0.010, ***p = 0.004, ****p < 0.001 using the Jonkheere-Terpstra test. Box and whisker plots show median and minimum to maximum values. Source of all embryos: Experiment 1.

Fig. 3: Immunostaining reveals increased proteotoxic stress, DNA-damage independent p53-activation, autophagy and apoptosis

a. Orthogonal projections after immunostaining of euploid and aneuploid embryos for DNA (white) and CASP3/7 (green). T= Trisomy, M=Monosomy. Source: Experiment 1. **b.** Orthogonal projections after immunostaining of euploid, aneuploid and reversine-treated embryos for DNA (white) and CASP8 (green). T= Trisomy. Source: Experiment 1. **c**. CASP3/7 mean intensity per cell. Euploid n=13, Aneuploid n=8 embryos. Unpaired t-test, *p = 0.0177. Source: Experiment 1. **d**. CASP8 mean intensity per cell. Euploid n=6, Aneuploid n=9, Reversine-treated n=8 embryos. One-way ANOVA, *p = 0.04, **p = 0.0098, ns= non-significant. Source: Experiment 1. **e**. Number of nuclei per embryo. Euploid n=26, Aneuploid n=29, Reversine-treated n=8 embryos. One-way ANOVA, ****p < 0.0001, **p = 0.0033, ns= non-significant. Source: Experiment 1 and 3. **f.** Orthogonal projections after immunostaining of euploid, aneuploid and reversine-treated embryos for DNA (white), LC3B (turquoise) and HSP70 (magenta). T= Trisomy. Source: Experiment 1. **g.** LC3B puncta per cell. Euploid n=19, Aneuploid n=22 embryos, Reversine-treated n=8 embryos. One-way ANOVA, **p = 0.0069, ***p = 0.0003, ns= non-significant. Source: Experiment 1. **h**. HSP70 mean intensity per cell. Euploid n=13, Aneuploid n=8, Reversine-treated n=8 embryos. One-way ANOVA, *p = 0.0121, **p = 0.0096, ns= non-significant. Source: Experiment 1. **i**. Orthogonal projections after immunostaining of euploid, aneuploid for DNA (white) and p62 (turquoise). White square shows zoom of a representative area. T= Trisomy, M=Monosomy. Source: Experiment 1. **j.** p62 puncta per cell. Euploid n=6, Aneuploid n=9 embryos. Unpaired t-test, *p = 0.0284. Source: Experiment 1. **k.** Optical sections of reversine treated embryos for DNA (white), CASP8 (green), HSP70 (red) showing cells with presence (yellow arrow) or absence (yellow arrowhead) of the proteins to

investigate co-localization. Source: Experiment 1. **l.** Percentage of cells of reversine embryos positive for either CASP8/HSP70, CASP8 or HSP70. One-way ANOVA, CASP8/HSP70 vs CASP8***p = 0.0003, CASP8/HSP70 vs HSP70***p = 0.0005, ns= non-significant. Source: Experiment 1. **m.** Orthogonal projections after immunostaining of euploid, aneuploid for DNA (white) and Serine (S) 15 p53 (turquoise). Source: Experiment 4. **n.** Percentage of Serine 15 p53 positive cells per embryo. Euploid n = 3, Aneuploid n = 5. Unpaired t-test with Welch's correction, *p = 0.0356. T= Trisomy. Source: Experiment 4. **o.** Orthogonal projections of immunostained untreated (n = 6) and Bleomycin treated (n = 6) embryos for DNA (white) and gH2AX (magenta) showing few foci in the untreated and pan-nuclear expression of gH2AX. Source: Experiment: 2. **p.** Orthogonal projections of immunostained euploid (n = 7) and aneuploid (n = 11) embryos for DNA (white), NANOG (green) and gH2AX (magenta). T= Trisomy. Source: Experiment 3. **q.** Percentage of cells with gH2AX foci or pan nuclear expression of euploid (n = 7) and aneuploid (n = 11) embryos in NANOG-negative, NANOG positive cells and whole embryos. Source: Experiment 3. **r.** Percentage of cells with gH2AX foci or pan nuclear expression of euploid (n = 7), low-dosage (n = 5) and high dosage (n = 6) aneuploid embryos in NANOG-negative, NANOG positive cells and whole embryos. Source: Experiment 3. **s.** Orthogonal projections of immunostained euploid (n = 6) and aneuploid (n = 11) embryos for DNA (white), DRAM1 (turquoise) and NANOG (green). T= Trisomy. Source: Experiment 3. **t.** DRAM1 mean cytoplasmatic intensity in TE and ICM of euploid and aneuploid cells. Euploid TE (n = 312 cells). Aneuploid TE (n = 434 cells). Euploid ICM (n = 43 cells). Aneuploid ICM (n = 70 cells). Each dot represents the cytoplasm of a single cell. One-way ANOVA, ****p<0.0001, ns = non-significant. Source: Experiment 3.

Embryo sources are indicated in each section. Brightfield pictures were obtained during confocal imaging. All scale bars are 20 μm. Box and whisker plots show median, and whiskers show minimum to maximum values. Bar plots and scatter plots show mean ± s.d.

Fig. 4: Aneuploid human embryos show less cells in trophectoderm and OCT4-positive cells and impaired lineage segregation events

a. Orthogonal projections after immunostaining of euploid (n = 7) and aneuploid embryos (n = 10) for DNA (white) and NANOG (green). T= Trisomy. Source: Experiment 3. **b.** NANOG nuclear enrichment in cells of the TE and ICM of euploid and aneuploid embryos. Each dot represents the nucleus of a single cell. Euploid TE (n = 718 cells). Aneuploid TE (n = 708 cells). Euploid ICM (n = 77 cells). Aneuploid ICM (n = 77 cells). **c.** Orthogonal projections after immunostaining of euploid and aneuploid embryos for DNA (white) and OCT4 (magenta). The first aneuploid panel (Trisomy 14 and 16) shows a similar number of ICM cells compared to the euploid embryo. The second aneuploid panel (Trisomy 14 and 22) shows an embryo without an ICM. T= Trisomy. Source: Experiment 4. **d**,**e**,**f**. Differences in number of nuclei per embryo between euploid and aneuploid embryos in the (**d**) OCT4-negative cells (trophectoderm) ***p = 0.0006 , (**e**) OCT4-positive cells (ICM/EPI), **p = 0.0055 and (**f**) whole embryo ***p = 0.0003. Euploid n = 16, Aneuploid n = 18. Unpaired t-test. Source: Experiment 4. **g.** Orthogonal projections after immunostaining of euploid and aneuploid embryos for DNA (white), CASP3/7 (green) and OCT4 (magenta). c. T= Trisomy, M= Monosomy. Yellow arrows indicate presence of the signal and yellow arrow heads indicate absence of signal. **h.** Percentage (%) of CASP3/7 positive (+) cells in the trophectoderm lineage (OCT4-negative cells). Euploid n = 9, Aneuploid n = 14. Unpaired t-test with Welch's correction, *p = 0.0453. Source: Experiment 4. **i**. CASP3/7 mean intensity per cell of whole embryos. Euploid n = 9, Aneuploid n = 14. Unpaired t-test with Welch's correction, *p = 0.0332. Source: Experiment 4. **j.** Left panel: Orthogonal projections after immunostaining of euploid and aneuploid embryos for DNA (white) and CASP3/7 (green) showing micronuclei. Yellow box indicates

zoomed-in region of interest (ROI). Yellow arrows indicate presence of micronuclei and overlap between DNA and CASP3/7. Source: Experiment 4. **k**, Number of micronuclei per cell in euploid and aneuploid whole embryos. Euploid n = 9, Aneuploid n = 14. Unpaired t-test with Welch's correction, *p = 0.0115. Source: Experiment 4. **l**. Orthogonal projections after immunostaining of euploid and aneuploid embryos for DNA (white), LC3B (turquoise) and OCT4 (magenta). Yellow circle indicates the ICM. The first aneuploid panel (Trisomy 1 and 20 and monosomy 18) shows OCT4-positive cells (ICM/EPI) with low levels of autophagy. The second aneuploid panel (Monosomy 14) shows an embryo with high levels of autophagy in the ICM. Source: Experiment 4. **m,n,o.** Differences in LC3B puncta per cell between euploid (n=10) and aneuploid (n=9) embryos in the (**m**) whole embryo, *p = 0.0220, (**n**) OCT4-negative cells (trophectoderm),*p = 0.0172 and (**o**) OCT4-positive cells (ICM/EPI) ns = non-significant. Mann-Whitney test. Source: Experiment 4. **p.** Orthogonal projections after immunostaining of euploid and aneuploid embryos for DNA (white), OCT4 (magenta) and GATA4 (green). The first aneuploid panel (trisomy 13 and 15) shows an embryo with presence of GATA4 positive cellc (PrE). The second aneuploid panel (Trisomy 7 and monosomies 5, 12 and 21) shows an embryo that did not contain GATA4 positive cells. Source: Experiment 4. **q.** Differences in the number of cells per embryo that were OCT4 positive and either GATA4 negative (magenta) or positive (green) or OCT4 negative and GATA4 positive (grey) between euploid (n=15) and aneuploid (n=18) embryos. In case GATA4-positive cells (PrE) were present we considered the GATA4-negative cells to be epiblast (EPI). All euploid embryos contained GATA4-positive cells, 7/18 aneuploid embryos had an ICM completely lacking GATA4-positive cells (Fisher-exact test, p = 0.009). **r**, Differences in the PrE/EPI ratio between euploid and aneuploid embryos that had an ICM containing GATA4-positive cells. Euploid n = 15,

Aneuploid n = 10. Unpaired t-test, **p = 0.0068. Source: Experiment 4. **s.** Violin plots with box plots of OCT4-positive-cells (ICM/EPI) per embryo (left, ns), OCT4-negative cells (trophectoderm) per embryo (center, ***p < 0.001) and GATA4-positive-cells (PrE) per embryo (right, ***p < 0.001, Jonkheere-Terpstra test) depending on gene dosage. Euploid (light blue), Low dosage (middle blue) and High dosage (darkest blue). Source: Experiment 4.

Brightfield pictures were obtained during confocal imaging. All scale bars are 20 µm. Box and whisker plots show median and minimum to maximum values. Bar plots show mean ± s.d. Besides (**b**) all dots represent one embryo.

Supplementary Fig. 1: Expanded RNA-sequencing analysis

a. Principal component analysis of reversine versus euploid embryos. **b.** InferCNV analysis of individual euploid samples compared to the reference set. **c.** InferCNV analysis of individual reversine samples compared to the reference set. **d**. Volcano plot after differential gene expression analysis with a cutoff value of $|\log_2 \text{fold change}| > 1$ and $-\log_{10}(\text{FDR}) < 0.05$ for reversine versus euploid embryos showing 34 upregulated and 22 downregulated genes. **e.** Barplot of enriched Hallmark pathways after gene set enrichment analysis of reversine versus euploid embryos using a cut-off value of 25% FDR. **f.** Barplot of TOP20 enriched C2 library pathways after gene set enrichment analysis of reversine versus euploid embryos using a cut-off value of 25% FDR. Source of all embryos: Experiment 1.

Supplementary Fig. 2: S15-p53 expression in TE vs OCT4-positive cells (ICM/EPI) in aneuploid embryos

a, Orthogonal projections after immunostaining of euploid and aneuploid embryos for DNA (white), S15p53 (turquoise) and OCT4 (magenta). **b**, Percentages of nuclei positive for S15p53 per embryo in euploid (n = 3) and aneuploid (n = 4) embryos in the ICM. **c**, Percentages of nuclei positive for S15p53 per embryo in euploid (n = 3) and aneuploid (n = 5) embryos in the TE.

Brightfield pictures were obtained during confocal imaging. All scale bars are 20 µm. Box and plots show median and minimum to maximum values. Bar plots show mean ± s.d. For all plots each dot represents a single embryo. Source of all embryos: Experiment 4.

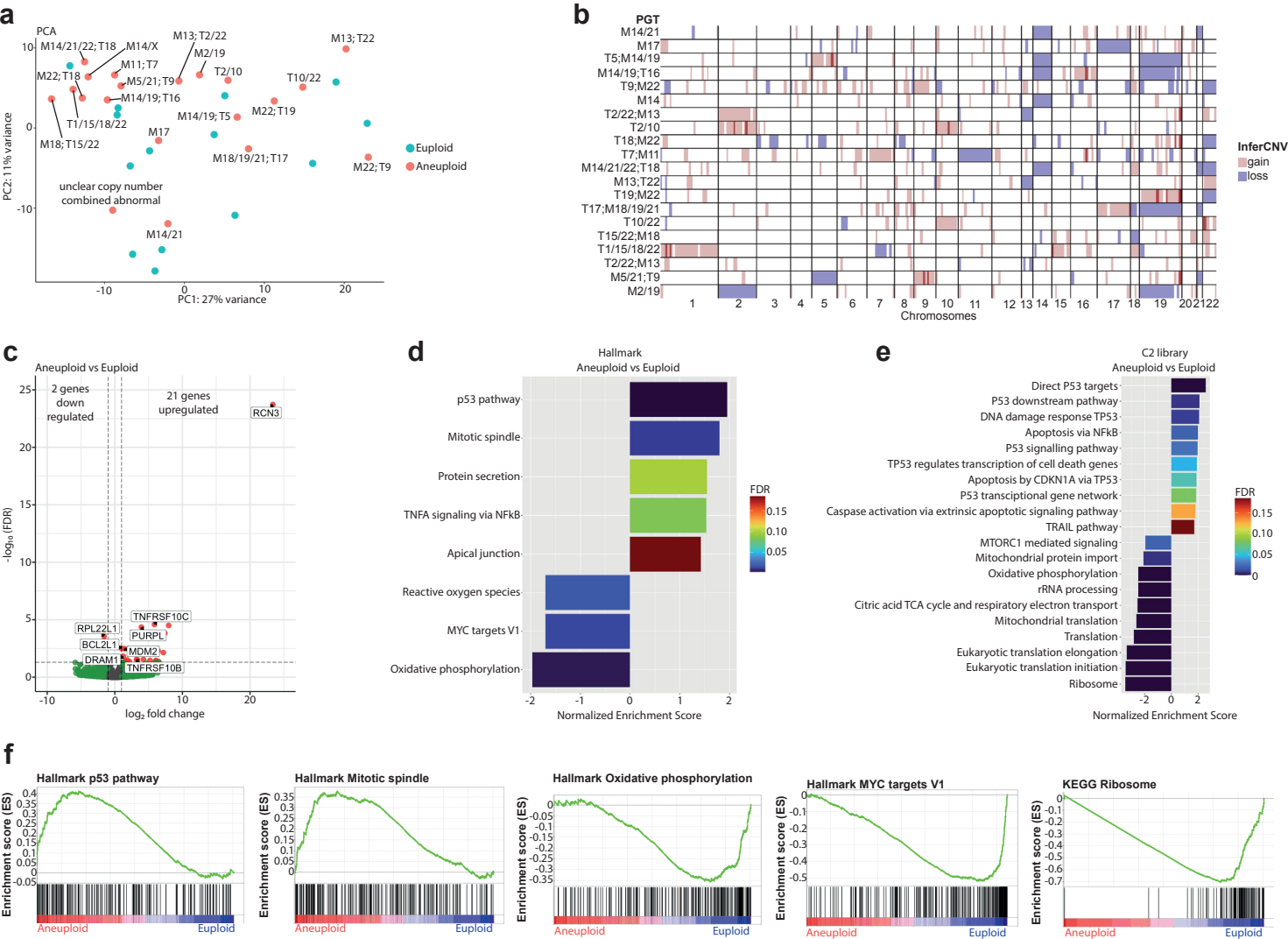
a
PCA
M14/21/22;T18
M14/X
M13;T2/22
M2/19
M13;T22
M11;T7
M22;T18
M5/21;T9
T2/10
T10/22
M14/19;T16
M14/19;T5
M22;T19
T1/15/18/22
M17
M18;T15/22
M18/19/21;T17
M22;T9
Euploid
Aneuploid
unclear copy number
combined abnormal
M14/21
PC2: 11% variance
PC1: 27% variance
b
PGT
M14/21
M17
T5;M14/19
M14/19;T16
T9;M22
M14
T2/22;M13
T2/10
T18;M22
T7;M11
M14/21/22;T18
M13;T22
T19;M22
T17;M18/19/21
T10/22
T15/22;M18
T1/15/18/22
T2/22;M13
M5/21;T9
M2/19
InferCNV
gain
loss
Chromosomes
c
Aneuploid vs Euploid
2 genes
down
regulated
21 genes
upregulated
RCN3
TNFRSF10C
RPL22L1
PURPL
BCL2L1
MDM2
DRAM1
TNFRSF10B
-log10 (FDR)
log2 fold change
d
Hallmark
Aneuploid vs Euploid
p53 pathway
Mitotic spindle
Protein secretion
TNFA signaling via NFkB
Apical junction
Reactive oxygen species
MYC targets V1
Oxidative phosphorylation
FDR
Normalized Enrichment Score
e
C2 library
Aneuploid vs Euploid
Direct P53 targets
P53 downstream pathway
DNA damage response TP53
Apoptosis via NFkB
P53 signalling pathway
TP53 regulates transcription of cell death genes
Apoptosis by CDKN1A via TP53
P53 transcriptional gene network
Caspase activation via extrinsic apoptotic signaling pathway
TRAIL pathway
MTORC1 mediated signaling
Mitochondrial protein import
Oxidative phosphorylation
rRNA processing
Citric acid TCA cycle and respiratory electron transport
Mitochondrial translation
Translation
Eukaryotic translation elongation
Eukaryotic translation initiation
Ribosome
FDR
Normalized Enrichment Score
f
Hallmark p53 pathway
Hallmark Mitotic spindle
Hallmark Oxidative phosphorylation
Hallmark MYC targets V1
KEGG Ribosome
Enrichment score (ES)
Aneuploid
Euploid

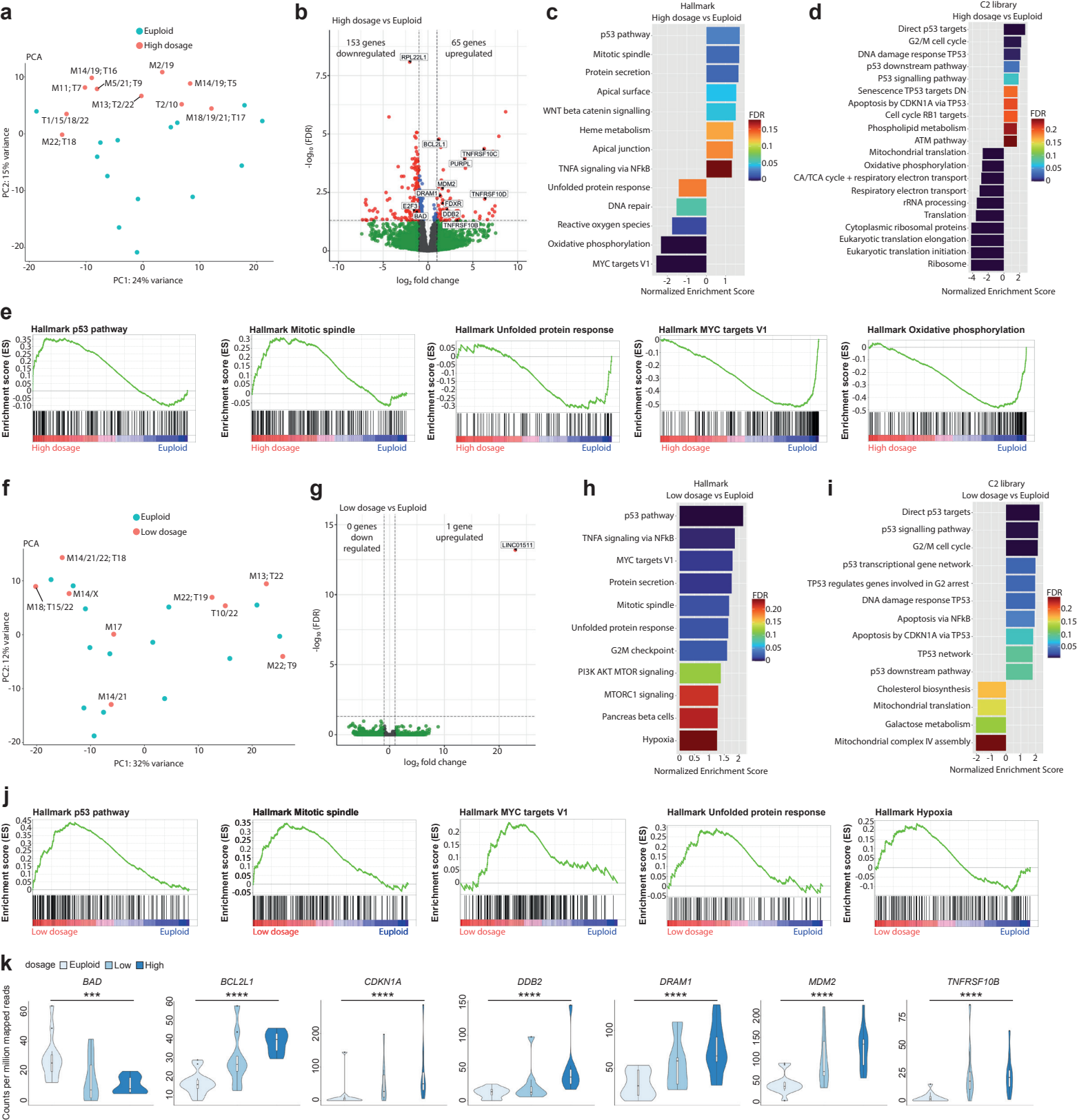
a
Euploid
High dosage
PCA
M14/19; T16
M2/19
M11; T7
M5/21; T9
M14/19; T5
M13; T2/22
T2/10
T1/15/18/22
M18/19/21; T17
M22; T18
PC2: 15% variance
PC1: 24% variance
b
High dosage vs Euploid
153 genes downregulated
65 genes upregulated
RPL22L1
BCL2L1
TNFRSF10C
PURPL
MDM2
DRAM1
TNFRSF10D
E2F3
FDXR
BAD
DDB2
TNFRSF10B
-log10 (FDR)
log2 fold change
c
Hallmark
High dosage vs Euploid
p53 pathway
Mitotic spindle
Protein secretion
Apical surface
WNT beta catenin signalling
Heme metabolism
Apical junction
TNFA signaling via NFkB
Unfolded protein response
DNA repair
Reactive oxygen species
Oxidative phosphorylation
MYC targets V1
FDR
Normalized Enrichment Score
d
C2 library
High dosage vs Euploid
Direct p53 targets
G2/M cell cycle
DNA damage response TP53
p53 downstream pathway
P53 signalling pathway
Senescence TP53 targets DN
Apoptosis by CDKN1A via TP53
Cell cycle RB1 targets
Phospholipid metabolism
ATM pathway
Mitochondrial translation
Oxidative phosphorylation
CA/TCA cycle + respiratory electron transport
Respiratory electron transport
rRNA processing
Translation
Cytoplasmic ribosomal proteins
Eukaryotic translation elongation
Eukaryotic translation initiation
Ribosome
FDR
Normalized Enrichment Score
e
Hallmark p53 pathway
Hallmark Mitotic spindle
Hallmark Unfolded protein response
Hallmark MYC targets V1
Hallmark Oxidative phosphorylation
Enrichment score (ES)
High dosage
Euploid
f
Euploid
Low dosage
PCA
M14/21/22; T18
M13; T22
M14/X
M18; T15/22
M22; T19
T10/22
M17
M22; T9
M14/21
PC2: 12% variance
PC1: 32% variance
g
Low dosage vs Euploid
0 genes down regulated
1 gene upregulated
LINC01511
-log10 (FDR)
log2 fold change
h
Hallmark
Low dosage vs Euploid
p53 pathway
TNFA signaling via NFkB
MYC targets V1
Protein secretion
Mitotic spindle
Unfolded protein response
G2M checkpoint
PI3K AKT MTOR signaling
MTORC1 signaling
Pancreas beta cells
Hypoxia
FDR
Normalized Enrichment Score
i
C2 library
Low dosage vs Euploid
Direct p53 targets
p53 signalling pathway
G2/M cell cycle
p53 transcriptional gene network
TP53 regulates genes involved in G2 arrest
DNA damage response TP53
Apoptosis via NFkB
Apoptosis by CDKN1A via TP53
TP53 network
p53 downstream pathway
Cholesterol biosynthesis
Mitochondrial translation
Galactose metabolism
Mitochondrial complex IV assembly
FDR
Normalized Enrichment Score
j
Hallmark p53 pathway
Hallmark Mitotic spindle
Hallmark MYC targets V1
Hallmark Unfolded protein response
Hallmark Hypoxia
Enrichment score (ES)
Low dosage
Euploid
k
dosage Euploid Low High
BAD
BCL2L1
CDKN1A
DDB2
DRAM1
MDM2
TNFRSF10B
Counts per million mapped reads

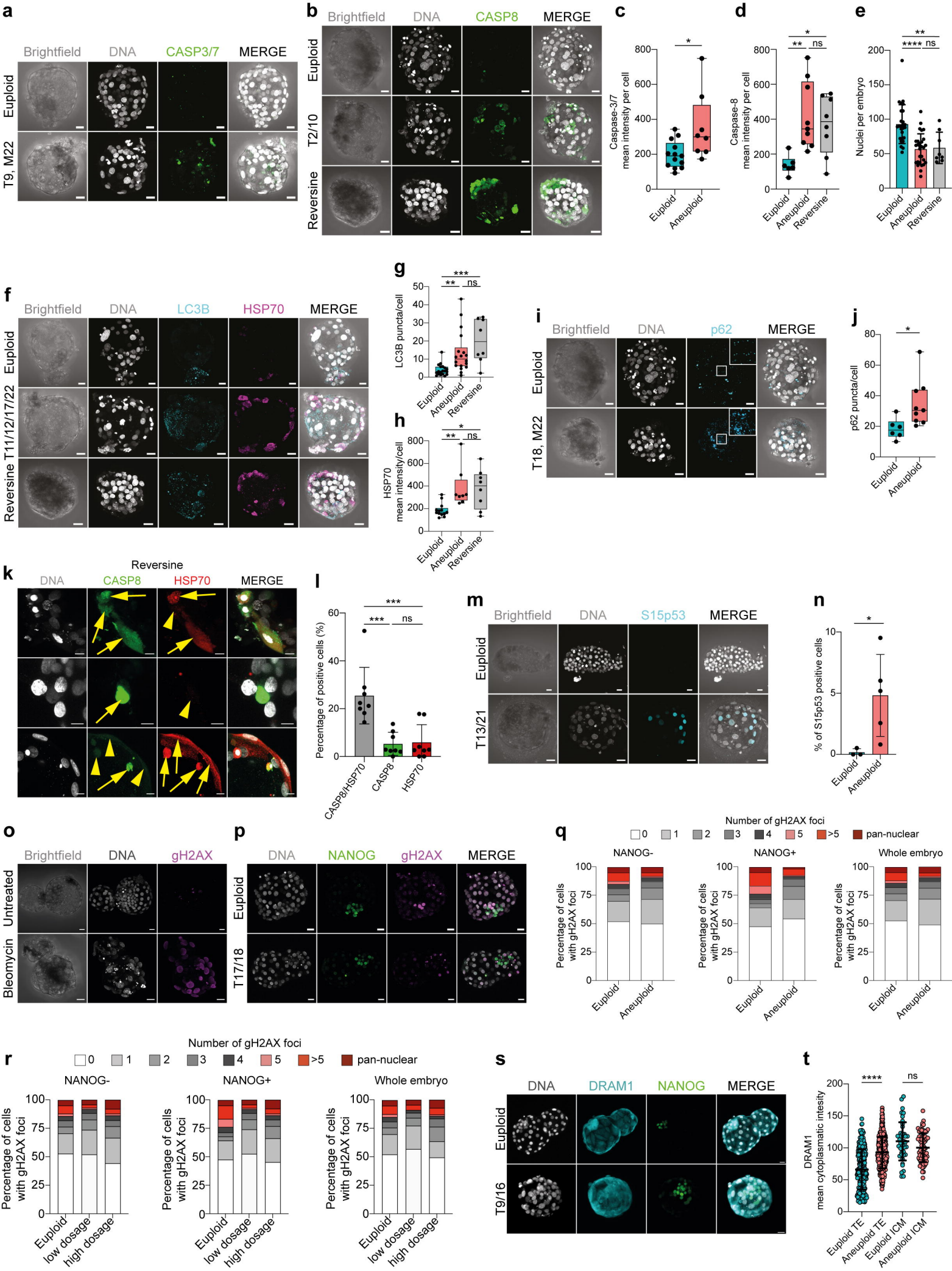
a
Brightfield
DNA
CASP3/7
MERGE
Euploid
T9, M22
b
Brightfield
DNA
CASP8
MERGE
Euploid
T2/10
Reversine
c
Caspase-3/7 mean intensity per cell
Euploid
Aneuploid
d
Caspase-8 mean intensity per cell
Euploid
Aneuploid
Reversine
e
Nuclei per embryo
Euploid
Aneuploid
Reversine
f
Brightfield
DNA
LC3B
HSP70
MERGE
Euploid
T11/12/17/22
Reversine
g
LC3B puncta/cell
Euploid
Aneuploid
Reversine
h
HSP70 mean intensity/cell
Euploid
Aneuploid
Reversine
i
Brightfield
DNA
p62
MERGE
Euploid
T18, M22
j
p62 puncta/cell
Euploid
Aneuploid
k
Reversine
DNA
CASP8
HSP70
MERGE
l
Percentage of positive cells (%)
CASP8/HSP70
CASP8
HSP70
m
Brightfield
DNA
S15p53
MERGE
Euploid
T13/21
n
% of S15p53 positive cells
Euploid
Aneuploid
o
Brightfield
DNA
gH2AX
Untreated
Bleomycin
p
DNA
NANOG
gH2AX
MERGE
Euploid
T17/18
q
Number of gH2AX foci
0
1
2
3
4
5
>5
pan-nuclear
NANOG-
NANOG+
Whole embryo
Percentage of cells with gH2AX foci
Euploid
Aneuploid
r
Number of gH2AX foci
0
1
2
3
4
5
>5
pan-nuclear
NANOG-
NANOG+
Whole embryo
Percentage of cells with gH2AX foci
Euploid
low dosage
high dosage
s
DNA
DRAM1
NANOG
MERGE
Euploid
T9/16
t
DRAM1 mean cytoplasmatic intesity
Euploid TE
Aneuploid TE
Euploid ICM
Aneuploid ICM

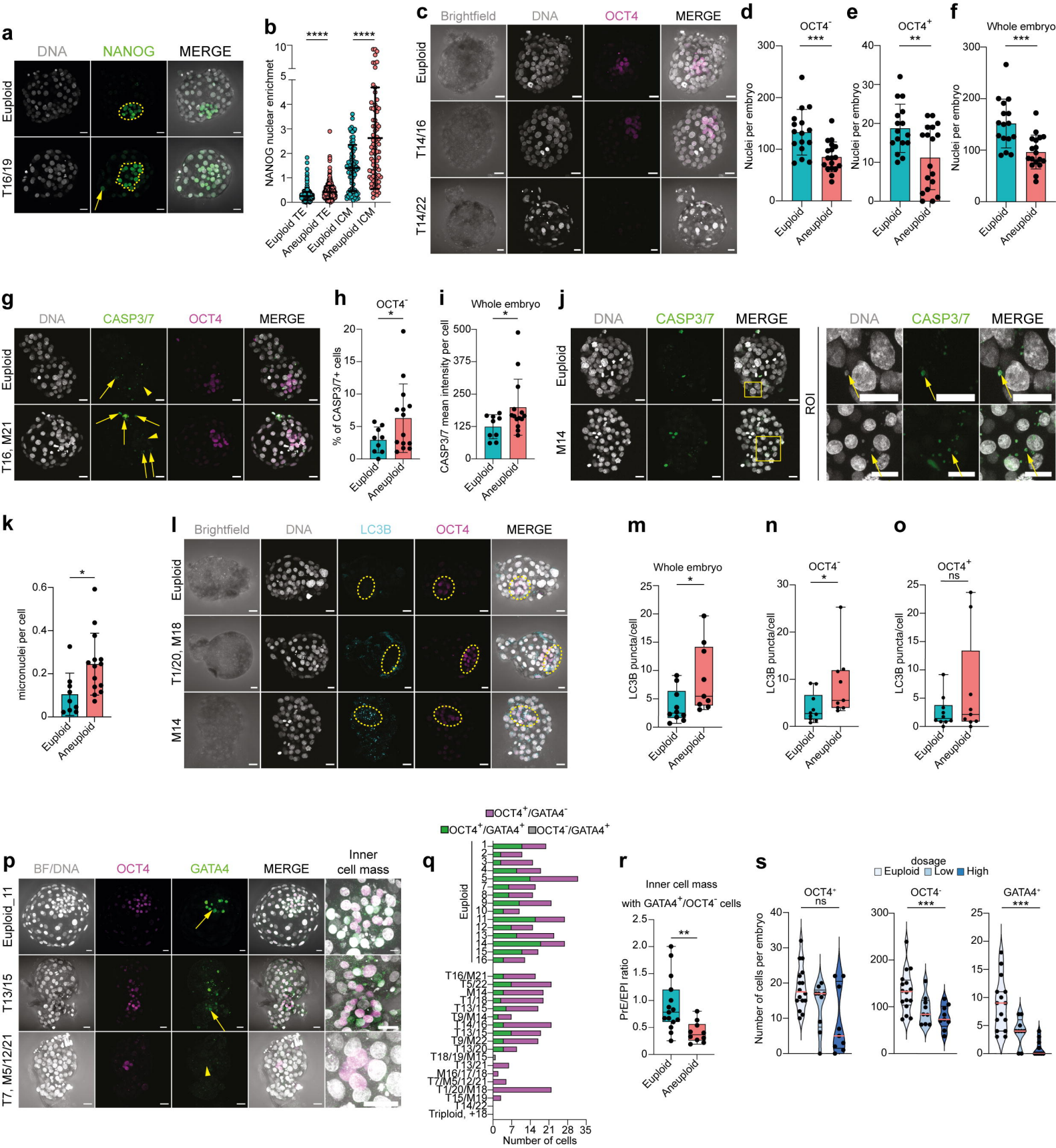
a
DNA
NANOG
MERGE
Euploid
T16/19
b
NANOG nuclear enrichmet
Euploid TE
Aneuploid TE
Euploid ICM
Aneuploid ICM
c
Brightfield
DNA
OCT4
MERGE
Euploid
T14/16
T14/22
d
OCT4⁻
Nuclei per embryo
Euploid
Aneuploid
e
OCT4⁺
f
Whole embryo
g
DNA
CASP3/7
OCT4
MERGE
Euploid
T16, M21
h
OCT4⁻
% of CASP3/7+ cells
i
Whole embryo
CASP3/7 mean intensity per cell
j
DNA
CASP3/7
MERGE
Euploid
M14
ROI
k
micronuclei per cell
l
Brightfield
DNA
LC3B
OCT4
MERGE
Euploid
T1/20, M18
M14
m
Whole embryo
LC3B puncta/cell
n
OCT4⁻
o
OCT4⁺
ns
p
BF/DNA
OCT4
GATA4
MERGE
Inner cell mass
Euploid_11
T13/15
T7, M5/12/21
q
OCT4⁺/GATA4⁻
OCT4⁺/GATA4⁺
OCT4⁻/GATA4⁺
Euploid
T16/M21
T5/22
M14
T1/18
T13/15
T9/M14
T14/16
T13/15
T9/M22
T13/20
T18/19/M15
T13/21
M16/17/18
T7/M5/12/21
T1/20/M18
T15/M19
T14/22
Triploid, +18
Number of cells
r
Inner cell mass
with GATA4⁺/OCT4⁻ cells
PrE/EPI ratio
s
dosage
Euploid
Low
High
OCT4⁺
ns
OCT4⁻
GATA4⁺
Number of cells per embryo

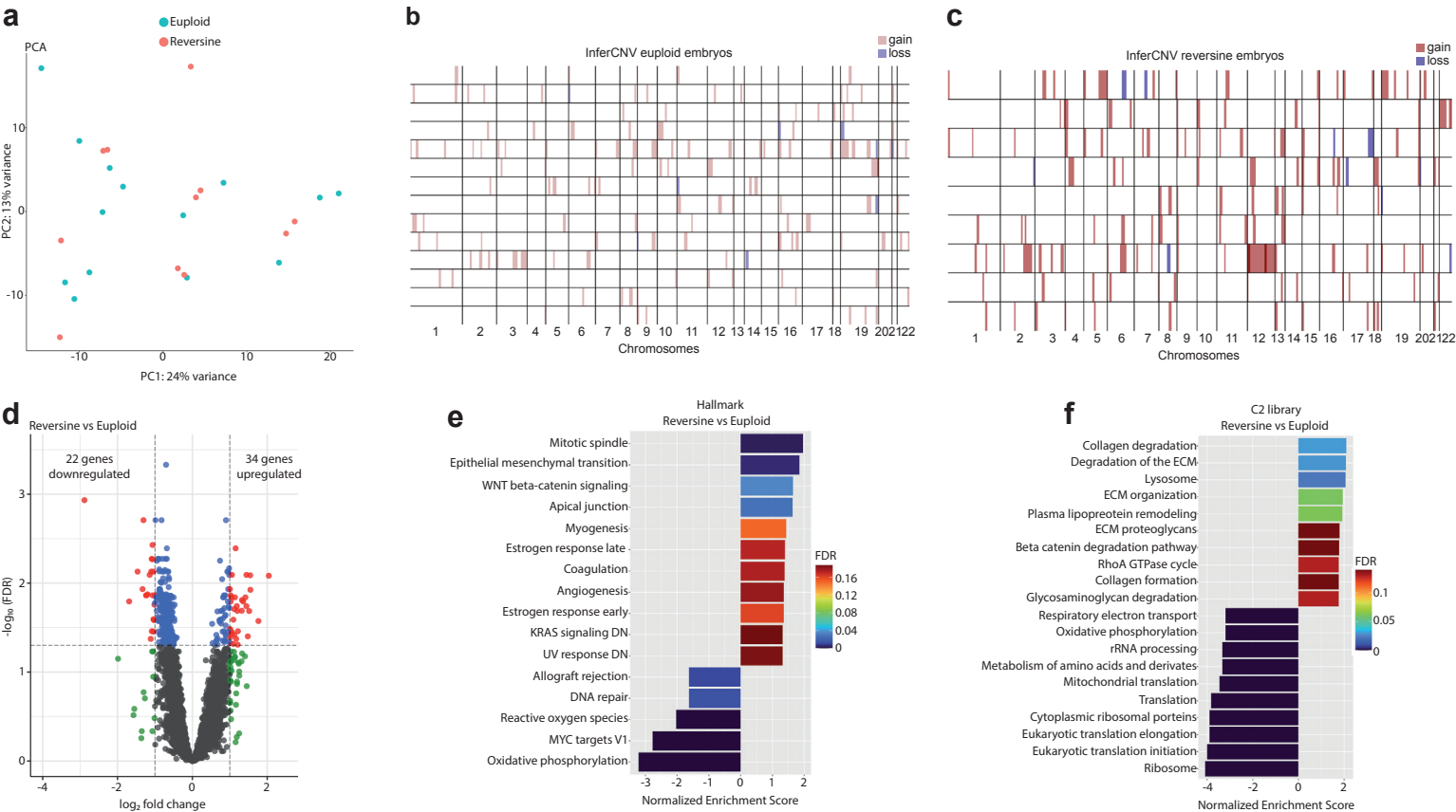
a
PCA
Euploid
Reversine
PC2: 13% variance
PC1: 24% variance
b
InferCNV euploid embryos
gain
loss
Chromosomes
c
InferCNV reversine embryos
gain
loss
Chromosomes
d
Reversine vs Euploid
22 genes downregulated
34 genes upregulated
-log10 (FDR)
log2 fold change
e
Hallmark
Reversine vs Euploid
Mitotic spindle
Epithelial mesenchymal transition
WNT beta-catenin signaling
Apical junction
Myogenesis
Estrogen response late
Coagulation
Angiogenesis
Estrogen response early
KRAS signaling DN
UV response DN
Allograft rejection
DNA repair
Reactive oxygen species
MYC targets V1
Oxidative phosphorylation
FDR
Normalized Enrichment Score
f
C2 library
Reversine vs Euploid
Collagen degradation
Degradation of the ECM
Lysosome
ECM organization
Plasma lipoprotein remodeling
ECM proteoglycans
Beta catenin degradation pathway
RhoA GTPase cycle
Collagen formation
Glycosaminoglycan degradation
Respiratory electron transport
Oxidative phosphorylation
rRNA processing
Metabolism of amino acids and derivates
Mitochondrial translation
Translation
Cytoplasmic ribosomal porteins
Eukaryotic translation elongation
Eukaryotic translation initiation
Ribosome
FDR
Normalized Enrichment Score

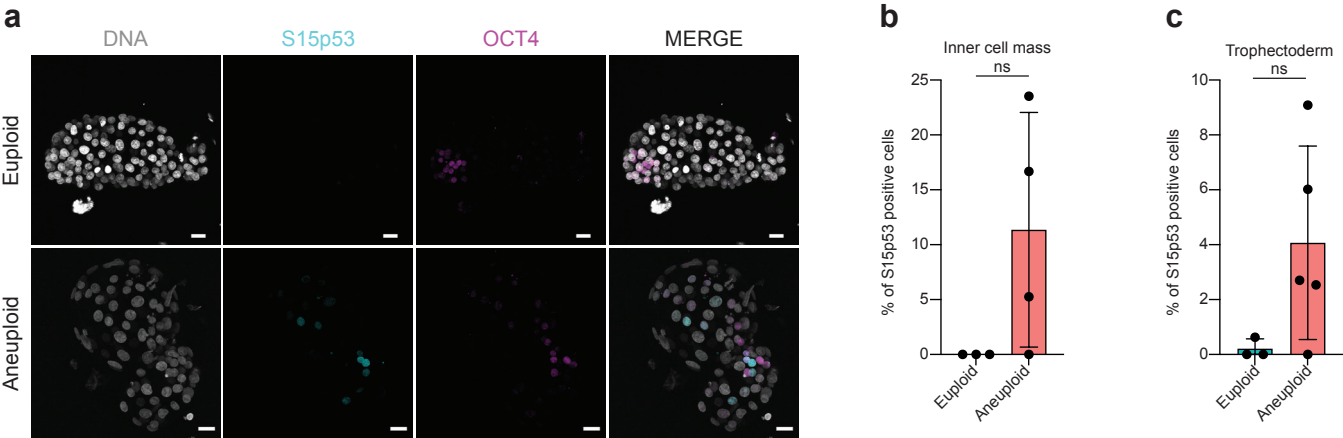
a
DNA
S15p53
OCT4
MERGE
Euploid
Aneuploid
b
Inner cell mass
ns
% of S15p53 positive cells
25
20
15
10
5
0
Euploid
Aneuploid
c
Trophectoderm
ns
% of S15p53 positive cells
10
8
6
4
2
0
Euploid
Aneuploid